An extended semi-analytical formulation for fast and reliable stress analysis of adhesively bonded joints

G. LELIAS[1,2,*], E. PAROISSIEN[1], F. LACHAUD[2], J. MORLIER[2], S. SCHWARTZ[1], and C. GAVOILLE[1]

[1]*SOGETI HIGH TECH, Parc le Millénaire - Bât A1, Avenue de l'Escadrille Normandie Niemen, 31700 BLAGNAC, FRANCE*

[2]*Institut Clément Ader, ISAE, Site de Rangeuil, 10 Avenue Edouard Belin, 31055 TOULOUSE Cedex 4, FRANCE*

Running Head: An extended semi-analytical formulation for fast and reliable stress analysis of adhesively bonded joints

*To whom correspondence should be addressed: Tel. +33534362684, Fax. +33534362626, E-mail: guillaume.lelias@sogeti.com

Abstract – The Finite Element (FE) method is able to address the stress analysis of adhesively bonded joints. However, analyses based on FE models are computationally expansive and it would be profitable to develop simplified approaches enabling extensive parametric studies. Firstly, a 1D-beam simplified model for the bonded joint stress analysis assuming a linear elastic adhesive material is presented. This model, derived from an approach inspired by the finite element (FE) method and based on the semi-analytical formulation of a 4-nodes macro-element, is able to simulate an entire bonded overlap. Secondly, a numerical procedure allowing for nonlinear adhesive stress-strain relationships to be accounted for is presented. This procedure allows for various non-linear adhesive behaviors (ie. softening, plastic, etc) to be accounted for with no restriction on the specimen geometry. The possible mixed-mode I/II response of the adhesive layer is introduced through an extension of the classical Cohesive Zone Modeling (CZM) procedure. This allows for various mixed mode criteria (ie. elliptic, Von-Mises, Benzeggagh-Kenane, etc) to be accounted for. The aforementioned procedure is illustrated using a bi-linear, an exponential, a polynomial and a perfectly plastic stress-strain evolution law. The results obtained by the simplified 1D-beam model are compared with time consuming 3D FE models predictions. Good agreement is shown.

keywords: *bonded joint, cohesive zone model, mixed-mode I/II, Finite Element method, semi-analytical formulation, macro-element*

NOMENCLATURE AND UNITS

A_j extensional stiffness (N) of the adherend j

B_j extensional and bending coupling stiffness (N.mm) of the adherend j

D_j bending stiffness (N.mm^2) of the adherend j

E Young's modulus (MPa) of the adhesive

E_j Young's modulus (MPa) of the adherend j

$\boldsymbol{F}$ vector of nodal forces

G Coulomb's modulus (MPa) of the adhesive

$\boldsymbol{K}$ stiffness matrix

$\boldsymbol{K_{BBe}}$ stiffness matrix of the Bonded-Beam macro-element

L length (mm) of the overlap

M_j bending moment (N.mm) in the adherend j around the z direction

N_j normal force (N) in the adherend j in the x direction

Q_σ nodal normal force (N) applied to the node σ in the x direction ($\sigma = i,j,k,l$)

$\boldsymbol{R}$ vector of imbalanced loads (N)

R_σ nodal shear force (N) applied to the node σ in the y direction ($\sigma = i,j,k,l$)

S adhesive peel stress (MPa)

S_σ nodal bending moment (N.mm) applied to the node σ around the z direction ($\sigma = i,j,k,l$)

T adhesive shear stress (MPa)

$\boldsymbol{U}$ vector of nodal displacements

V_j shear force (N) in the adherend j in the y direction

b width (mm) of the adherends

e thickness (mm) of the adhesive

e_j thickness (mm) of the adherend j

n number of macro-elements

u_j displacement (mm) of the adherend j in the x direction

u_a displacement (mm) of the node a in the x direction ($a = i,j,k,l$)

w_j displacement (mm) of the adherend j in the y direction

w_a displacement (mm) of the node a in the y direction ($a = i,j,k,l$)

Δ length (mm) of a macro-element

η characteristic constant

ρ characteristic constant

ν_j Poisson's ratio of the adherend j

θ_j angular displacement (rad) of the adherend j around the z direction

θ_a angular displacement (rad) of the node a around the z direction ($a = i,j,k,l$)

(x,y,z) system of coordinates

1. INTRODUCTION

1.1. Context

In the frame of the design of structural components, the choice of joining technologies is essential. Adhesive bonding can be considered as an attractive joining technology, compared to conventional ones, such as bolting or riveting. Indeed, adhesive bonding offers the possibility of joining without damaging various combinations of materials, including plastics and metals. Moreover, since the amount of adhesive required to sustain static or fatigue loads is very low, adhesive bonding allows for weight benefits. However, the interest of adhesive bonding remains while the integrity of the joint is ensured. To take advantage of adhesive bonding, accurate strength predictions are thus required.

The strength prediction of bonded joints requires the determination of computed criteria and experimentally characterized allowable. Several approaches are proposed in the open literature. These approaches could besides be used in the experimental characterization process of allowable.

The stress analysis approach, based on the Strength of Materials, is the classical approach. It aims at localizing the maximal values of stresses and strains, as highlighted in several literature surveys [1-4]. Another approach is based on the Fracture Mechanics. Assuming the presence of an initial crack, judiciously localized and sized by the user, it allows for the computation of strain energy release rate or J-integral parameters at crack tip as a function of applied forces or adhesive stresses [4-7]. In the coupled stress and energy criterion approach, the crack length at initiation is not assumed but derived from the analysis [8-9]. Then, the computed crack length at initiation is not a material characteristic and depends both on geometrical parameters as well as on material critical stress and energy release rate. Finally, the Cohesive Zone Modeling – denoted CZM – is

based on Damage Mechanics. It enables a diagnostic of the current damage state and an update of the strength prediction. The damage, associated to micro-cracks or voids, results in a progressive degradation of the material stiffness before failure. Both damage initiation and propagation phases are included in the formulation, without assuming any initial cracks [10-12]. Experimental approaches based on classical Fracture Mechanics tests allow for the characterization of the mechanical constitutive cohesive behavior of adhesive layers [13-14].

1.2. Objective

The Finite Element – denoted FE – method is able to address the stress, fracture and damage analyses of bonded joints [4]. Nevertheless, since analyses based on FE models are computationally expansive, it would be profitable both to restrict them to refined analyses and to develop for designers simplified approaches, enabling extensive parametric studies. The objective of this paper is then to present a simplified approach for the mixed-mode I/II non-linear analysis of adhesively bonded joints.

A large number of simplified approaches for the stress analysis of bonded joints exist in the open literature [1-3]. The joint kinematic is then simplified. The displacement field of adherends is supposed relevant to the beam or plate theory while the adhesive displacement field is expressed in terms of that of adherends, then restricting the number of components of the adhesive stress tensor. A widespread modeling of the adhesive layer consists in an elastic foundation, supporting both adherend interfaces [15-16]. The adhesive stresses are then function of the relative displacements of the adherend interfaces, which is consistent with the CZM. Depending on the additional simplifying hypotheses taken, a closed-form solution is not always available, so that mathematical procedures [17-19] are needed to integrate the governing system of differential equations in view of boundary conditions.

The semi-analytical solution presented in [19] considers the adherends as Euler-Bernoulli laminated beams supported by an infinite number of elastic shear and peel springs.

Besides, an original procedure allowing for non-linear adhesive behaviors to be accounted for is presented. However, the authors show that the aforementioned procedure is theoretically limited to the analysis of single-lap joint configurations only.

In the present paper, a reworked semi-analytical procedure enabling for various non-linear adhesive behaviors to be accounted for with no restriction on the specimen geometry is presented. The possible mixed mode I/II response of the adhesive layer is introduced through an extension of the classical CZM procedure [10-13]. The semi-analytical procedure is illustrated using a bi-linear softening, an exponential softening, a polynomial softening and a perfectly plastic adhesive stress-strain evolution law. The results obtained with the simplified 1D-beam model are then compared with the results obtained from both theoretical and 3D FE analyses.

1.3. Overview of the paper

In a first part, for lecturer comfort, the description of the linear elastic 1D-beam model for the stress analysis of a single-lap bonded joint is provided. In a second part, an original procedure allowing for the mixed-mode I/II response of the adhesive layer to be addressed is presented. In the third part, an iterative procedure based on an adaptation of the classical Newton-Raphson convergence scheme, and allowing for various non-linear adhesive stress-strain relationships to be accounted for is presented and developed in view of its implementation. Finally, the results obtained from the simplified 1D-beam model are compared with those of 3D FE models involving interface elements.

2. LINEAR ELASTIC 1D-BEAM MODEL

2.1. Overview

The simplified linear elastic method is inspired by the FE method and allows for the resolution of the bonded overlap system of governing differential equations. The

displacements and forces of both adherends, as well as the adhesive stresses, are then computed. The method consists in meshing the structure. A fully bonded overlap is meshed using a unique 4-nodes macro-element, which is specially formulated to allow for the resolution of the bonded overlap system of governing differential equations. For convenience, this macro-element is thereafter referred as the Bonded-Beam (BBe) element. The outer adherends are meshed using classical Euler-Bernoulli beam elements. According to the classical FE rules, the stiffness matrix of the entire structure – termed ***K*** – is assembled and the selected boundary conditions are applied. The minimization of the total potential energy is then ensured by solving the equation ***F=KU***, where ***F*** is the vector of nodal forces and ***U*** the vector of nodal displacements. This approach based on the use of BBe elements takes the advantage of the flexibility of the FE method and allows for the semi-analytical resolution of the bonded overlap system of differential equations at low computational costs. Indeed, by using BBe elements as elementary bricks, it offers the possibility to simulate complex structures involving single-lap bonded joints at low computational costs [20].

2.2. Formulation of the BBe element

2.2.1. Hypotheses. The model is based on the following hypotheses: (i) the thickness of the adhesive layer is constant along the overlap, (ii) the adherends are simulated by linear elastic Euler-Bernoulli laminated beams, and (iii) the adhesive layer is simulated by an infinite number of elastic shear and peel springs linking both adherends. Note that (iv) the adherend shear stress can possibly be assumed as varying linearly with the adherend thickness.

2.2.2. Governing differential equations. The local equilibrium of both adherends (see Fig.1) leads to the following system of six equations:

$$\begin{cases} \dfrac{dN_j}{bdx} = (-1)^j T \\ \dfrac{dV_j}{bdx} = (-1)^{j+1} S \qquad , \quad j = 1,2 \\ \dfrac{dM_j}{dx} + V_i + \dfrac{e_j}{2} bT = 0 \end{cases} \tag{1}$$

where S is the adhesive peel stress, T the adhesive shear stress, N_1 (N_2) the normal force in the adherend 1 (2), V_1 (V_2) the shearing force in the adherend 1 (2) and M_1 (M_2) the bending moment in the adherend 1 (2).

This local equilibrium is the one derived and employed by Goland and Reissner [16] in their classical theory. Furthermore, considering possible extensional and bending coupling stiffnesses in the adherends, the constitutive equations are expressed as:

$$\begin{cases} N_j = A_j \dfrac{du_j}{dx} - B_j \dfrac{d^2 w_j}{dx^2} \\ M_j = -B_j \dfrac{du_j}{dx} + D_j \dfrac{d^2 w_j}{dx^2}, \quad j = 1,2 \\ \theta_j = \dfrac{dw_j}{dx} \end{cases} \tag{2}$$

with A_j the extensional stiffness, B_j the coupling stiffness, and D_j the bending stiffness of the adherend j (j=1,2). For demonstration purpose it is assumed that $\Delta_j = A_j D_j - B_j^2$ is not equal to zero. The adhesive is considered as linear elastic and is simulated by an infinite number of elastic shear and elastic peel springs. The adhesive shear stress and the adhesive peel stress are then expressed as:

$$\begin{cases} T = \dfrac{G}{e}\left(u_2 - u_1 - \dfrac{1}{2} e_1 \theta_1 - \dfrac{1}{2} e_2 \theta_2 \right) \\ S = \dfrac{E}{e}\left(w_1 - w_2 \right) \end{cases} \tag{3}$$

where E is the peel modulus of the adhesive, G the shear modulus of the adhesive, u_1 (u_2) the normal displacement of the adherend 1 (2), w_1 (w_2) the transverse deflection of the adherend 1 (2), and θ_1 (θ_2) the bending angle of the adherend 1 (2).

2.2.3. Stiffness Matrix of the BBe element.

System of differential equations in terms of adhesive stresses. Equation (2) is written as:

$$\begin{cases} \dfrac{du_j}{dx} = \dfrac{D_j N_j + B_j M_j}{\Delta_j} \\ \dfrac{d^2 w_j}{dx^2} = \dfrac{A_j M_j + B_j N_j}{\Delta_j} \end{cases} , j = 1,2 \qquad (4)$$

By combining equations (1) to (4), the following linear differential equation system in terms of adhesive stresses is obtained:

$$\begin{cases} \dfrac{d^3 T}{dx^3} = k_1 \dfrac{dT}{dx} + k_2 S \\ \dfrac{d^4 S}{dx^4} = -k_4 S - k_3 \dfrac{dT}{dx} \end{cases} \qquad (5)$$

where:

$$\begin{cases} k_1 = \dfrac{Gb}{e}\left[\dfrac{D_1}{\Delta_1}\left(1 + \dfrac{A_1 {e_1}^2}{4D_1}\right) + \dfrac{D_2}{\Delta_2}\left(1 + \dfrac{A_2 {e_2}^2}{4D_2}\right) + \left(\dfrac{e_1 B_1}{\Delta_1} - \dfrac{e_2 B_2}{\Delta_2}\right)\right] \\ k_2 = \dfrac{Gb}{e}\left[\dfrac{e_1 A_1}{2\Delta_1} - \dfrac{e_2 A_2}{2\Delta_2} + \left(\dfrac{B_1}{\Delta_1} + \dfrac{B_2}{\Delta_2}\right)\right] \\ k_3 = \dfrac{Eb}{e}\left[\dfrac{e_1 A_1}{2\Delta_1} - \dfrac{e_2 A_2}{2\Delta_2} + \left(\dfrac{B_1}{\Delta_1} + \dfrac{B_2}{\Delta_2}\right)\right] \\ k_4 = \dfrac{Eb}{e}\left[\dfrac{A_1}{\Delta_1} + \dfrac{A_2}{\Delta_2}\right] \end{cases} \qquad (6)$$

By successive differentiations and linear combinations, the system of differential equations (5) can be uncoupled as:

$$\begin{cases} \dfrac{d^6 S}{dx^6} - k_1 \dfrac{d^4 S}{dx^4} + k_4 \dfrac{d^2 S}{dx^2} + S(k_2 k_3 - k_1 k_4) = 0 \\ \dfrac{d}{dx}\left(\dfrac{d^6 T}{dx^6} - k_1 \dfrac{d^4 T}{dx^4} + k_4 \dfrac{d^2 T}{dx^2} + T(k_2 k_3 - k_1 k_4)\right) = 0 \end{cases} \qquad (7)$$

The system (7) is then solved and the adhesive shear and peel stresses are written as:

$$\begin{cases} S(x) = \left[\begin{array}{l} \overline{K_1} e^{sx}\sin(tx) + \overline{K_2} e^{sx}\cos(tx) + \overline{K_3} e^{-sx}\sin(tx) \\ + \overline{K_4} e^{-sx}\cos(tx) + \overline{K_5} e^{rx} + \overline{K_6} e^{-rx} \end{array}\right] \\ T(x) = \left[\begin{array}{l} K_1 e^{sx}\sin(tx) + K_2 e^{sx}\cos(tx) + K_3 e^{-sx}\sin(tx) \\ + K_4 e^{-sx}\cos(tx) + K_5 e^{rx} + K_6 e^{-rx} + K_7 \end{array}\right] \end{cases} \tag{8}$$

Nodal displacements and forces. The determination of the stiffness matrix of BBe element requires the determination of both nodal displacements and nodal forces (see Fig.2). Following the resolution scheme introduced in [21], the displacements (forces) in each adherend are expressed as functions of both the adhesive stresses and their derivatives. The computation of the displacements (forces) of each adherend is fully detailed in [18]. However it is shown that the entire problem is dependent on a total number of 12 integration constants only:

$${}^{t}\mathrm{C} = \begin{pmatrix} K_1 & K_2 & K_3 & K_4 & K_5 & K_6 & K_7 & J_1 & J_2 & J_3 & J_5 & J_7 \end{pmatrix} \tag{9}$$

The nodal displacements (forces) are then computed from the values of displacements (forces) at $x=0$ and $x=\Delta$. It is shown that the nodal displacements (forces) are linearly dependent on the 12 integration constants listed in (9), through a coupling parameter matrix $\boldsymbol{M}$ ($\boldsymbol{N}$):

$$\mathbf{U} = \begin{pmatrix} u_i \\ u_j \\ u_k \\ u_l \\ w_i \\ w_j \\ w_k \\ w_l \\ \theta_i \\ \theta_j \\ \theta_k \\ \theta_l \end{pmatrix} = \begin{pmatrix} u_1(0) \\ u_2(0) \\ u_1(\Delta) \\ u_2(\Delta) \\ w_1(0) \\ w_2(0) \\ w_1(\Delta) \\ w_2(\Delta) \\ \theta_1(0) \\ \theta_2(0) \\ \theta_1(\Delta) \\ \theta_2(\Delta) \end{pmatrix} = \mathbf{MC} \quad \textit{and} \quad \mathbf{F} = \begin{pmatrix} Q_i \\ Q_j \\ Q_k \\ Q_l \\ R_i \\ R_j \\ R_k \\ R_l \\ S_i \\ S_j \\ S_k \\ S_l \end{pmatrix} = \begin{pmatrix} -N_1(0) \\ -N_2(0) \\ N_1(\Delta) \\ N_2(\Delta) \\ -V_1(0) \\ -V_2(0) \\ V_1(\Delta) \\ V_2(\Delta) \\ -M_1(0) \\ -M_2(0) \\ M_1(\Delta) \\ M_2(\Delta) \end{pmatrix} = \mathbf{NC} \tag{10}$$

where Q, R and S respectively refer to the nodal normal forces, shearing forces and bending moments acting on the BBe element.

Stiffness matrix. Classically, the coefficients of the stiffness matrix are obtained by differentiating each component of the nodal forces by each component of the nodal displacements:

$$\mathbf{K}_{\mathbf{BBe}} = \begin{pmatrix} \left[\frac{\partial Q_\sigma}{\partial u_\tau}\right] & \left[\frac{\partial Q_\sigma}{\partial w_\tau}\right] & \left[\frac{\partial Q_\sigma}{\partial \theta_\tau}\right] \\ \left[\frac{\partial R_\sigma}{\partial u_\tau}\right] & \left[\frac{\partial R_\sigma}{\partial w_\tau}\right] & \left[\frac{\partial R_\sigma}{\partial \theta_\tau}\right] \\ \left[\frac{\partial S_\sigma}{\partial u_\tau}\right] & \left[\frac{\partial S_\sigma}{\partial w_\tau}\right] & \left[\frac{\partial S_\sigma}{\partial \theta_\tau}\right] \end{pmatrix} \quad ,\sigma,\tau = i,j,k,l \tag{11}$$

so that:

$$\mathbf{F} = \mathbf{K}_{\mathbf{BBe}}\mathbf{U} \tag{12}$$

But, considering the expression for the vector of nodal forces (***F***) as a function of the vector of integration constants (***C***) as well as the vector ***C*** as a function of the vector of nodal displacements (***U***), the stiffness matrix of the BBe element can be computed as follows:

$$\mathbf{K}_{\mathbf{BBe}} = \mathbf{N}\mathbf{M}^{-1} \tag{13}$$

The stiffness matrix of the entire structure – termed ***K*** – is then assembled from both the elementary stiffness matrix $\boldsymbol{K_{BBe}}$ and the elementary stiffness matrix of the Euler-Bernoulli laminated beam elements (see Appendix.1).

3. SEMI-ANALYTICAL COHESIVE ZONE MODELING

In this section, the adhesive layer is assumed to have a non-linear behavior. To take into account the non-linear behavior of the adhesive layer, an iterative procedure derived from the classical FE theory [22] is presented. The possible mixed-mode I/II response of various non-linear adhesive behaviors is then addressed through an extension of the classical CZM procedure [10-13]. This procedure allows for various non-linear adhesive

behaviors and (or) mixed-mode criteria to be accounted for with no restriction on the specimen geometry.

3.1. Mixed-mode modeling

In the present paper, a particular emphasis is given to the modeling of 3 softening and 1 perfectly plastic adhesive behaviors (see Fig.3). However the given procedure is not limited to these particular behaviors only, and can easily applies to coupled elasto-plasto-damaging behaviors. For convenience, the adhesive stress-strain relationship is thereafter referred as the adhesive traction-separation law.

3.1.1. Description of the mixed-mode I/II adhesive behavior. Because of the 1D-beam foundation of the BBe element system of governing differential equations, it is necessary to account for the possible mixed-mode I/II response of the specimen. The mixed-mode I/II response of such structures can be accounted for through the definition of the following parameters:

$$\begin{cases} \beta = \dfrac{\delta_{II}}{\delta_I} \\ \delta_m = \sqrt{\delta_I^2 + \delta_{II}^2} \end{cases} \tag{14}$$

where β, δ_I, δ_{II}, δ_m, respectively refer to the mixed-mode ratio, the peeling deformation, the shearing deformation and the mixed-mode deformation of the adhesive layer. A schematic representation of those parameters is given in Fig.4.

3.1.2. Description of the pure modes adhesive behavior. The basic idea of mixed-mode modeling is to combine pure mode traction-separation laws through both initiation and propagation criteria. The effective properties of the adhesive layer traction-separation laws are then computed with respect to those initiation and propagation criteria. Numbers of those criteria can be found in the open literature (see Tab.1). To allow for the combination of the pure mode traction-separation laws, both the elastic energy (Y_{0i})

and the fracture energy (G_{Ci}) of pure modes i ($i=I,II$) are generally required. A mathematical description of such pure modes is then needed (see Tab.2-3).

3.1.3. Combination of the pure modes adhesive behavior. To compute the effective properties of the pure mode traction separation laws, both the elastic energy ($Y_{0,mi}$) and fracture energy ($G_{C,mi}$) of the pure mode projections of the mixed-mode traction-separation law have to be computed (see Fig.4). Since the shape of the projected traction-separations laws is assumed as identic as the initial pure mode traction-separation laws, the elastic and fracture energies of the projected traction-separation laws ($Y_{0,mi}$, $G_{C,mi}$) can be derived from the expression of the pure mode elastic and fracture energies ($Y_{0,i}$, $G_{C,i}$) by changing the subscript i in mi. Considering the projected elastic and fracture energies ($Y_{0,mi}$, $G_{C,mi}$) as a function of the effective pure mode traction-separation thresholds ($\delta_{0,mi}$, $\delta_{C,mi}$), both initiation/propagation criteria can be expressed in the form of:

$$F_k\left(\delta_{0,mi},\delta_{C,mi},k_i,\delta_{0,i},\delta_{C,i},\beta\right)=0 \quad \begin{matrix} ,i=I,II \\ ,k=0,C \end{matrix} \tag{15}$$

where $F_k(\delta_{0,mi},\delta_{C,mi},k_i,\delta_{0,i},\delta_{C,i},\beta)$ refers to a function of the effective initiation/propagation thresholds ($\delta_{0,mi}$, $\delta_{C,mi}$), the mixed-mode ration (β), and the initial pure mode properties (k_i, $\delta_{0,i}$, $\delta_{C,i}$).

Since simple algebraic expressions of the effective initiation/propagation thresholds cannot be always written [13], an iterative procedure based on the false position method is derived to compute those pure mode projections of the mixed-mode traction-separation law. Assuming two initial sets of physically acceptable test values (***a***, ***b***), the solution of the problem $F_k(\delta_{0,mi},\delta_{C,mi},k_i,\delta_{0,i},\delta_{C,i},\beta)=0$ is iteratively approached using the root of the secant line between ($\boldsymbol{a}$, $F(\boldsymbol{a})$) and ($\boldsymbol{b}$, $F(\boldsymbol{b})$) (see Fig.5). The given procedure allows for the effective pure mode properties ($\delta_{0,mi}$, $\delta_{C,mi}$) for various non-linear adhesive stress-strain evolution laws and (or) initiation/propagation criteria, to be computed from both the mixed-mode ratio (β) and the initial pure mode properties (k_i, $\delta_{0,i}$, $\delta_{C,i}$).

3.2. Non-linear iterative convergence scheme (Numerical approach)

3.1.1. Overview of the Newton-Raphson procedure. The Newton-Raphson procedure is a numerical procedure which allows for the root of non-linear equations to be iteratively approached. The method consists in building a vector series $\boldsymbol{X}^n$ converging towards the solution $\boldsymbol{X}$ of a non-linear problem $F(\boldsymbol{X})=0$. To allow for the next iteration $\boldsymbol{X}^{n+1}$ to be computed from the knowledge of $\boldsymbol{X}^n$, the function $F(\boldsymbol{X})$ is approached by its first order Taylor expansion around $\boldsymbol{X}^n$ such that:

$$0 \approx F\left(\mathbf{X}^{n+1}\right) = F\left(\mathbf{X}^{n}\right) + F'\left(\mathbf{X}^{n}\right)\left(\mathbf{X}^{n+1} - \mathbf{X}^{n}\right) \tag{16}$$

Assuming $\boldsymbol{X}^{n+1}$ as satisfying $F(\boldsymbol{X}^{n+1})\approx 0$, the next iteration $\boldsymbol{X}^{n+1}$ can be computed as follows:

$$\mathbf{X}^{n+1} = \mathbf{X}^{n} - \left[F'\left(\mathbf{X}^{n}\right)\right]^{-1} F\left(\mathbf{X}^{n}\right) \tag{17}$$

Where $F'(\boldsymbol{X})$ refers to the tangent linear application associated with the function $F(\boldsymbol{X})$. Then, the exact value of $F(\boldsymbol{X}^{n+1})$ is recomputed and the function $F(\boldsymbol{X})$ relinearized using its first order Taylor expansion around $\boldsymbol{X}^{n+1}$. The given procedure is then repeated until the difference between two following iterations falls below a given convergence criterion. The recomputation of $F(\boldsymbol{X}^{n+1})$ is generally referred as the projection step. In the case of linear applications, the derivative $F'(\boldsymbol{X})$ is referred as the Jacobian matrix of $F(\boldsymbol{X})$ at point $\boldsymbol{X}$.

One of the greatest advantages of the Newton-Raphson procedure is that the convergence rate near to the solution $\boldsymbol{X}$ is quadratic. However, the use of this procedure requires the computation of the tangent linear application at each convergence step, implying time-consuming computations, possible divergence of the algorithm and (or) numerical issues.

Since the computation of the Newton-Raphson iteration $\boldsymbol{X}^{n+1}$ has not necessarily to be approached using the first order Taylor expansion of $F(\boldsymbol{X})$, numbers of authors suggests the use of other linear elastic applications. These modified procedures are referred as quasi Newton-Raphson procedures.

3.1.2. Global equilibrium of the joint. Because of the FE like formulation of the BBe element, the global equilibrium of the bonded overlap can be expressed in the form of:

$$\delta\Pi = 0 = \delta\mathbf{U}^T\mathbf{K}_S\mathbf{U} - \delta\mathbf{U}^T\mathbf{F}_{ext} \quad (18)$$

where $\boldsymbol{K_S}$ refers to the secant stiffness matrix, $\boldsymbol{U}$ to the vector of nodal displacements and $\boldsymbol{F_{ext}}$ to the applied nodal forces defined in section 2. The given equilibrium condition derives from the application of the Principle of Virtual Work and applies to each BBe element.

3.1.3. Adaptation of the Newton-Raphson procedure

Adaptation of the general Newton-Raphson procedure. As presented in the previous section, the equilibrium condition of the BBe element is given in equation (18). Note that the given condition individually applies to each BBe element. The following demonstration then refers to the equilibrium condition of a unique BBe element and can be easily extended to the entire structure using the classical assembly FE rules.

Assuming that $\delta\boldsymbol{U}^T$ as kinematically acceptable, the aforementioned equilibrium can be expressed as:

$$\mathbf{L}^{int}(\mathbf{U}) = \mathbf{L}^{ext}(\mathbf{U}) \quad (19)$$

where $\boldsymbol{L^{int}}=\boldsymbol{K_sU}$ and $\boldsymbol{L^{ext}}=\boldsymbol{F_{ext}}$ respectively refer to the internal reactions and the external forces acting on the BBe element. Note that in the general case, both $\boldsymbol{L^{int}}$ and $\boldsymbol{L^{ext}}$ depend on the vector of nodal displacements $\boldsymbol{U}$. Considering that no *following forces*[1], such as load pressure or centrifugal forces, are applied to the joint, $\boldsymbol{L^{ext}}$ does not depend on the vector of nodal displacements $\boldsymbol{U}$.

The expression of the element equilibrium can then be simplified as:

$$\mathbf{L}^{int}(\mathbf{U}) = \mathbf{L}^{ext} \quad (20)$$

[1] Following forces – Forces that depend on the vector of nodal displacement (ie. load pressure, centrifugal forces, etc).

Defining the linear application *R* as the difference between $\boldsymbol{L}^{int}$ and $\boldsymbol{L}^{ext}$, the research of the solution of the element equilibrium can be reduced to the research of the root of $R(\boldsymbol{U})=0$. For convenience, the linear application $R(\boldsymbol{U})$ will be thereafter referred as the vector of imbalanced loads.

$$R(\mathbf{U}) = 0 = \mathbf{L}^{\mathbf{int}}(\mathbf{U}) - \mathbf{L}^{\mathbf{ext}} \tag{21}$$

The research of the solution of the non-linear problem $R(\boldsymbol{U})=0$ can thus be seen as a direct application of the Newton-Raphson procedure. Considering $\boldsymbol{U}^n$ as an increasingly better estimation of the equilibrium solution $\boldsymbol{U}$, the next iteration $\boldsymbol{U}^{n+1}$ can be computed as follows:

$$\mathbf{U}^{n+1} = \mathbf{U}^n - \left[R'(\mathbf{U}^n)\right]^{-1} R(\mathbf{U}^n) \tag{22}$$

Within the original Newton-Raphson procedure, the tangent linear application $F'(X)$ has to be computed at each convergence iteration. In equation (22), $R'(\boldsymbol{U})$ refers to the tangent linear application associatied with $R(\boldsymbol{U})$. In the absence of *following forces*[1], the tangent linear application $R'(\underline{\boldsymbol{U}})$ can be expressed as:

$$R'(\mathbf{U}^n) = \left.\frac{\partial \mathbf{L}^{\mathbf{int}}}{\partial \mathbf{U}}\right|_{\mathbf{U}^n} - \left.\frac{\partial \mathbf{L}^{\mathbf{ext}}}{\partial \mathbf{U}}\right|_{\mathbf{U}^n} = \left.\frac{\partial \mathbf{L}^{\mathbf{int}}}{\partial \mathbf{U}}\right|_{\mathbf{U}^n} \tag{23}$$

where the derivative of $\boldsymbol{L}^{int}$ refers to the Jacobian matrix of the linear application $\boldsymbol{L}^{int}=\boldsymbol{K}_S\boldsymbol{U}$ (26). Note that if *following forces*[1] are applied to the joint, the tangent linear application $R'(\boldsymbol{U})$ cannot be reduced to the single derivative of $\boldsymbol{L}^{int}$.

$$\left.\frac{\partial \mathbf{L}^{\mathbf{int}}}{\partial \mathbf{U}}\right|_{\mathbf{U}^n} = \left.\frac{\partial}{\partial \mathbf{U}}\mathbf{K}_{\mathbf{S}}\mathbf{U}\right|_{\mathbf{U}^n} = \begin{bmatrix} \left.\frac{\partial L_1^{\mathrm{int}}}{\partial U_1}\right|_{\mathbf{U}^n} & \cdots & \left.\frac{\partial L_1^{\mathrm{int}}}{\partial U_k}\right|_{\mathbf{U}^n} \\ & \ddots & \\ \left.\frac{\partial L_k^{\mathrm{int}}}{\partial U_1}\right|_{\mathbf{U}^n} & \cdots & \left.\frac{\partial L_k^{\mathrm{int}}}{\partial U_k}\right|_{\mathbf{U}^n} \end{bmatrix} \tag{24}$$

However, as the secant stiffness matrix $\boldsymbol{K}_S$ depends on the BBe element nodal displacement $\boldsymbol{U}$, the exact computation of the tangent linear application is not possible. The tangent linear application $R'(\boldsymbol{U})$ can be at best approached using the definition of the tangent linear growth rate of $\boldsymbol{L}^{int}$ (equation (25)).

$$\left.\frac{\partial L_i^{\text{int}}}{\partial U_j}\right|_{\mathbf{U}^n} = \frac{L_i^{\text{int}}\left(\mathbf{U}^{n-1} + U_j^n\right) - L_i^{\text{int}}\left(\mathbf{U}^{n-1}\right)}{U_j^n - U_j^{n-1}} \quad ,i,j = 1,\ldots,k \tag{25}$$

As a result of the complexity of the computation of the tangent linear application (the Newton-Raphson iterations must be sufficiently small to justify the use of the tangent linear growth rate of $\boldsymbol{L^{int}}$), it is decided to focus on quasi Newton-Raphson procedures.

Computation of the vector of imbalanced loads. Since the exact computation of the imbalance load vector highly determines the convergence of the series $\boldsymbol{U}^n$ toward the equilibrium solution $\boldsymbol{U}$, a particular attention has to be given to its correct estimation. As previously presented, the imbalance load vector is defined as the difference between the vectors of internal reactions $\boldsymbol{L^{int}}$ and applied forces $\boldsymbol{L^{ext}}$ acting on the BBe element (equation (21)).

The vector of internal reactions $\boldsymbol{L^{int}}=\boldsymbol{K_S U}$ can then be computed from both the secant stiffness matrix $\boldsymbol{K_S}$ of the BBe element and the vector of nodal displacements $\boldsymbol{U}$. However, the secant stiffness matrix is defined on a set of constant adhesive peel and shear moduli (see Section.2). Since the projection of the adhesive stresses can lead to dissimilar left side and right side adhesive secant stiffnesses (see Fig.6), it is decided to update the secant stiffness matrix using the averaged peel and shear moduli along the element.

The vector $\boldsymbol{L^{ext}}=\boldsymbol{F_{ext}}$ can in turn be computed from the external forces applied to the BBe element. Using the definition of the secant stiffness matrix $\boldsymbol{K_S}$, $\boldsymbol{L^{ext}}$ can be expressed from the secant stiffness matrix at iteration $\boldsymbol{U}^{n-1}$ and the vector of the BBe element nodal displacements at iteration $\boldsymbol{U}^n$.

Finally, the vector of imbalanced loads $R(\boldsymbol{U})$ can be expressed in the form of:

$$R(\mathbf{U}) = \mathbf{K}_{\mathbf{S}}\left(\mathbf{U}^{n-1}\right)\mathbf{U}^n - \mathbf{K}_{\mathbf{S}}\left(\mathbf{U}^n\right)\mathbf{U}^n \tag{26}$$

Implementation of modified Newton-Raphson procedures. By discretizing the adhesive overlap with an adequate number of BBe element, it is then possible to address the non-linear response of the adhesive layer so that:

1. Initialization of the first iteration of the vector of nodal displacements ($\boldsymbol{U}=\boldsymbol{0}$)
2. Computation of the initial elastic stiffness matrix of each element
3. Assembly of the initial elastic stiffness matrix of the entire structure ($\boldsymbol{K}$)
4. Assembly of the vector of applied loads ($\boldsymbol{F}$)
5. Initialization of the vector of imbalanced loads ($\boldsymbol{R}=-\boldsymbol{F}$)
6. Computation of the first/next iteration of vector $\boldsymbol{U}$ ($\boldsymbol{U}^{n+1}=\boldsymbol{U}^{n}-\boldsymbol{K}^{-1}\boldsymbol{R}$)
7. Computation of the mixed-mode traction-separation parameters
8. Projection of the adhesive stresses (T, S) with respect to the computed effective traction-separation properties.
9. Computation of the updated secant stiffness matrix of each element
10. Assembly of the updated secant stiffness matrix of the entire structure ($\boldsymbol{K}$)
11. Computation of the updated vector of imbalanced loads ($\boldsymbol{R}$)

(Repeat steps 6 to 11 until a given convergence criterion is satisfied)

4. COMPARISON WITH FINITE ELEMENT PREDICTIONS

4.1. Description of the Finite Element models

The mechanical response of three adhesive joint specimens is investigated (ENF[2], DCB[3] & MMB[4]). Those specimens are characteristic of pure mode I, pure mode II and mixed-mode adhesive solicitations, and have been widely used for the mechanical characterization of adhesive interfaces [23-24]. A schematic representation of each specimen is presented in Fig.7. The geometry of each specimen is balanced. The

[2] ENF – End Notched Flexure specimen. Allows for the pure mode II adhesive characterization.
[3] DCB – Double Cantilever Beam specimen. Allows for the pure mode I adhesive characterization.
[4] MMB – Mixed Mode Bending specimen. Allows for mixed-mode I/II adhesive characterization.

simulations are performed using SAMCEF FE Code v14-1.02. Both adherends are modeled as facing purely linear elastic deformations only. To obtain a width independent distribution of stresses, the y-axis displacement field is fixed to zero. To account for the Poison's effect, the effective properties of each adherend are here considered (see Tab.4). The adhesive layer is modeled using a bi-linear cohesive traction-separation law. Both linear energetic initiation and propagation criteria are assumed (see Tab.5).

The adherends are meshed using 3D brick SAMCEF type T008 elements. The degree of the elements is 1. SAMCEF type T008 elements have linear interpolation functions and 9 internal modes (ie. 8 nodes and 24 degrees of freedom). The normal integration scheme is chosen. The adhesive interface is meshed using 2D cohesive interface SAMCEF type T146 elements. The degree of the elements is 1. SAMCEF type T146 elements have linear interpolation functions and no internal modes (ie. 4 nodes and 8 degrees of freedom). Because of numerical convergence issues, the Gauss-Lobatto integration scheme is here chosen [27]. Loads and boundary conditions are applied to the neutral fiber of each adherend.

4.2. Convergence of the Finite Element models

To allow for the comparison of converged results, the mesh of each FE models is optimized so that the solution obtained is independent on the mesh refinement. The optimization of the mesh is based on the following hypotheses: (i) the mesh of the specimen is uniformly distributed over the length, the width and the thickness of the adherends, (ii) the mesh of the upper adherend, the adhesive interface, and the lower adherend are corresponding, (iii) the aspect ratio of each element of the structure is equal to 1. It is shown from hypotheses (i) to (iii) that the mesh of the entire specimen is then dependent on the number of elements within the length of the adhesively bonded overlap only (see Appendix.2).

4.3. Description of the semi-analytical models

A schematic representation of the semi-analytical models is presented in Fig.8. The adhesive overlap is meshed using *n* uniformly distributed BBe elements. The outer adherends are meshed using a unique Euler-Bernoulli beam element. Both adherends are modeled as monolithic beams. The adhesive layer is modeled using a bi-linear cohesive traction-separation law. Both linear energetic initiation and propagation criteria are assumed.

4.4. Convergence of the semi-analytical models

As presented in section 2, when facing purely linear elastic deformations, the adhesive overlap can be modeled using a unique 4-nodes BBe element. However, the aforementioned procedure needs the adhesive overlap to be meshed with an adequate number of BBe elements to address the correct non-linear behavior of the adhesive layer. Since the adhesive overlap has to be meshed, the results obtained can depend on its refinement. To allow for the comparison of converged results, the overlap mesh is then optimized so that the solution obtained is independent on its refinement (see Appendix.2).

4.5. Comparison with Finite Element predictions

The End-Notched Flexure specimen. Fig.9 presents the comparison between semi-analytical results and Finite Element predictions in term of load versus displacement curve (a), distribution of adhesive stresses (b) and distribution of the damage variable (c) along the overlap. Good agreement is shown with Finite Element predictions.

The Double Cantilever Beam specimen. Fig.10 presents the comparison between semi-analytical results and Finite Element predictions in term of load versus displacement

curve (a), distribution of adhesive stresses (b) and distribution of the damage variable (c) along the overlap. Good agreement is shown with Finite Element predictions.

The Mixed-Mode Bending specimen. Fig.11 presents the comparison between semi-analytical results and Finite Element predictions in term of load versus displacement curve (a), distribution of adhesive stresses (b) and distribution of the damage variable (c) along the overlap. Good agreement is shown with Finite Element predictions.

6. CONCLUSION AND DISCUSSION

In the present paper, an original procedure derived from the FE method is adapted to the particular formulation of the BBe element. The procedure allows for various non-linear adhesive behaviors to be accounted for (ie. softening, plastic, etc) with no restriction on the specimen geometry. A general procedure allowing for the effective mixed-mode I/II properties of the adhesive layer to be accounted for is presented. A particular attention is given to the modeling of 3 types of cohesive damage and 1 perfectly plastic evolution laws (see Fig.3). However the aforementioned procedure is not limited to these particular behaviors only. Note that the procedure has been recently adapted to coupled elastoplastic-damaging behaviors and extended to user-defined adhesive traction-separation laws.

The mechanical response of three classical Fracture Mechanics adhesive specimens is investigated (ie. ENF[2], DCB[3] & MMB[4]). It is seen from Fig.9-11 that semi-analytical results are in extremely good agreement with classical 3D Finite Element strength predictions (during both initiation and propagation phases). The suggested simplified joint kinematic is then shown as consistent with the simulation of the mechanical response of the investigated specimens. Since the ENF[2], DCB[3] and MMB[4] specimens are representative of either pure mode I, pure mode II and mixed-mode I/II adhesive solicitations, it is legitimate to think that the simplified joint kinematic will be consistent

with the mechanical analysis of other pure mode or mixed-mode I/II adhesive joint specimens, such as bSLJ[5], IbSLJ[6], CLS[7], T-Stiff[8], etc.

When facing purely linear-elastic deformations, the semi-analytical results are shown as independent on the mesh refinement (see Fig.A2-1 and Fig.A2-2). This independency on the mesh refinement is due to the specific formulation of the BBe element and allows for linear elastic bonded overlaps to be modeled using a unique 4-nodes BBe. However, when facing non-linear deformations, the semi-analytical results are shown as dependent on the mesh refinement. To account for the non-linear behavior of the adhesive layer the adhesive overlap has then to be meshed with an adequate number of BBe elements. However, it is shown that the results obtained are rapidly converging toward an asymptote (see Fig.A2-3 and Fig.A2-4). On the contrary, the 3D Finite Element predictions are shown as dependent on the mesh refinement in the case of both linear-elastic and non-linear deformations (see Fig.A2-5, Fig.A2-6, Fig.A2-7, and Fig.A2-2). Moreover, in the case of non-linear analyses, FE results are shown as not clearly converging toward an asymptote (see Fig.10-11). According to the authors of the present paper, these slight variations of the FE predictions result from the choice of inherent convergence criterion (ie. Newton-Raphson iteration scheme).

By the suggested simplified joint kinematic, it is shown that the mechanical response of a large range of bonded overlaps can be simulated using a restricted number of elements (ie. only one when facing linear-elastic deformations only). Each of those elements is specifically formulated and allows for the modeling of adhesively bonded overlaps at low computational costs. This approach based on the use of BBe elements thus takes the advantage of the flexibility of FE methods (ie. wide application range, simple assembly procedure, account of the boundary conditions, specific linear and non-linear resolution schemes, etc.) and the robustness of theoretical approaches (ie. analytical resolution of the set of governing differential equations, results independent on the mesh refinement

[5] bSLJ – balanced Single-Lap Joint
[6] IbSLJ – imbalanced Single-Lap Joint
[7] CLS – Cracked-Lap Shear
[8] T-Stiff – T-Stiffener

when facing linear-elastic adhesive deformations, results shown as rapidly converging toward an asymptote when facing non-linear adhesive deformations, etc.).

Since no simplifying assumptions are made on the joint kinematic in classical 3D FE analyses, converged FE results generally imply highly refined meshes and time-consuming computations. However the use of specially formulated elements, such as BBe elements, allows for the mechanical analyses of such specimens with a restricted number of elements, and so degrees of freedom. It is shown from Fig.12 that the gain in term of degrees of freedom involved in the problem can vary from a factor 15 to 35, depending on the specimen geometry (ie. ENF[2], DCB[3] and MMB[4]).

Using BBe elements as elementary bricks of larger models also offer the possibility to simulate more complex structures involving single-lap bonded overlaps at low computational costs.

As shown as consistent with classical FE predictions of either pure mode I, pure mode II and mixed-mode I/II adhesive specimens, the suggested approach thus finds it interest in many extensive parametric studies and/or experimental characterization techniques of adhesively bonded joints (ie. allowing fast and reliable adhesive stress analyses for extensive parametric studies and/or inverse characterization techniques).

ACKNOWLEDGMENT

G. LELIAS, E. PAROISSIEN, S. SCHWARTZ and C. GAVOILLE gratefully acknowledge the support from the SOGETI HIGH TECH engineers and managers involved in the development of JoSAT (Joint Stress Analysis Tool) internal research program, and in particular Mr VASSE for his help during the study of the influence of the mesh refinement on 3D FE models.

REFERENCES

1. JW van Ingen, and A Vlot. Stress analysis of adhesively bonded single lap joints. (Report LR-740). Delft University of Technology (April 1993).

2. MY Tsai, and J Morton. An evaluation of analytical and numerical solutions to the single-lap joint. Int J Solids Structures. 31, pp. 2537-2563 (1994).

3. LFM da Silva, PJC das Neves, RD Adams, and JK Spelt. Analytical models of adhesively bonded joints-Part I: Literature survey. Int J Adhesion Adhesives. 29, pp. 319-330 (2009).

4. LFM da Silva, and RDSG Campilho. Advances in numerical Modelling of adhesive joints. SpringerBriefss in Applied Sciences and Technology, Publisher: Springer Berlin Heidelberg, pp. 1-93 (2012).

5. P Fraise and F SCHIMT. Use of J-integral as fracture parameter in simplified analysis of bonded joints. Int J Fracture. 63, pp. 59-73 (1993).

6. L Tong. Bond shear strength for adhesive bonded double-lap joints. Int J Solids Structures. 31(21), pp. 2919-2931 (1994).

7. G Fernlund. Stress analysis of bonded lap joints using fracture mechanics and energy balance. Int J Solids Structures. 27, pp. 574-592 (2007).

8. D Leguillon. Strength or toughness? A criterion for crack onset at a notch. European Journal of Mechanics-A/Solids 21 (1), pp. 61-72 (2002).

9. P Weissgraeber and W Becker. Finite Fracture Mechanics model for mixed mode fracture in adhesive joints. Int. J Solids Structures (2013).

10. N Valoroso, and L Champaney. A damage model for simulating decohesion in adhesively bonded assemblies. Proceeding to ECCOMAS 2004, Jyväskyä, FI (July 2004).

11. MFSF de Moura, JPM Gonçalves, JAG CHOUSAL, and Campilho RDSG. Cohesive and continuum mixed-mode damage models applied to the simulation of the mechanical behavior of bonded joints. Int J Adhesion Adhesives. 28, pp. 419-426 (2008).

12. RDSG Campilho, MD Benea, JABP Neto, LFM Da Silva. Modeling adhesive with cohesive zone models: effects of the cohesive law shape of the adhesive layer. Int J of Adhesion and Adhesives. Vol 44, pp. 48-56 (2013).

13. KN Anyfantis. Analysis and design of composite-to-metal adhesively bonded joints. PhD thesis. National Technical University of Athens, School of Naval Architecture and Marine Engineering (2012).

14. A Biel. Mechanical behavior of adhesive layers. PhD Thesis. Chalmers University of Technology, Göteborg, Sweden (2008).

15. O Volkersen. Die Nietkraftverteilung in Zugbeanspruchten Nietverbindungen mit konstanten Laschenquerschnitten. Luftfahrtforschung, Vol. 15, pp. 41-47 (1938).

16. M Goland, and E Reissner. The stresses in cemented joints. J App Mech. Trans. ASME. 11, pp. A17-A27 (1944).

17. E Oterkus, A Barut, E Madenci, SS Smeltzer III, and DR Ambur. Nonlinear analysis of bonded composite single-lap joints. Paper presented at: 45th AIAA/ASME/ASCE/AHS/ASC Structures, Structural Dynamics & Materials Conference, Palm Springs, CA (April 2004).

18. F Mortensen. Development of tools for engineering analysis and design of high-performance FRP-composite structural elements. PhD Thesis. Aalborg University, Denmark (1998).

19. E Paroissien, F Lachaud, and T Jacobs. A simplified stress analysis of bonded joints using macro-elements. In: *Advanced in Modeling and Design of Adhesively Bonded Systems*. S Kumar and KL Mittal (Eds.), Scrivener Publishing, Wiley, pp. 93-146 (2013).

20. SE Stapleton. The analysis of adhesively bonded advanced composite joints using joint finite elements. PhD thesis. University of Michigan (2012).

21. JL Högberg. Mechanical behavior of single-layer adhesive joints – An integrated approach. Thesis for the degree of licentiate of engineering. Chalmers University of Technology, Göteborg, Sweden (2004).

22. M Abbas. Algorithm for non-linear quasi-statique analysis. R5.03.01. Code Aster. User's Manual (2013).

23. M Kenane, ML Benzeggagh. Mixed mode delamination fracture toughness of unidirectional glass-epoxy composites under fatigue loadings. Composite Science & Technology. Vol 57, pp. 597-605 (1997).

24. JR Reeder ; An evaluation of mixed mode delamination criteria. NASA Technical report 104210 (1992).

25. AD Crocombe, H Khoramuishad, KB Katnam, IA Ashcroft. A generalized damage model for constant amplitude fatigue loading of adhesively bonded joints. Int J of Adhesive & Adhesion. 30, pp. 513-522 (2010).

26. L Champaney. Outils de conception et d'analyse pour les assemblages de structures complexes. HdR Thesis. Université de Versailles St Quentin en Yvelines (2004).

27. SAMCEF. SAMCEF v14.10-2. User's manual (2013).

LIST OF FIGURE CAPTIONS

Figure A1-1. Assembly of the single-lap joint configuration. Linear elastic 1D-beam model.

Figure A2-1. Evolution of the maximum displacement at loaded nodes as a function of the number of elements within the length of the adhesive bondline. Convergence of the solution facing linear-elastic deformations. Convergence of the Finite Element models.

Figure A2-2. Evolution of the adhesive peel and shear stresses at crack tip as a function of the number of elements within the length of the adhesive bondline. Convergence of the solution facing linear-elastic adhesive deformations. Convergence of the Finite Element models.

Figure A2-3. Evolution of the maximum displacement at loaded nodes as a function of the number of elements within the length of the adhesive bondline. Convergence of the solution facing non-linear adhesive deformations. Convergence of the Finite Element models.

Figure A2-4. Evolution of the adhesive peel and shear stresses at crack tip as a function of the number of elements within the length of the adhesive bondline. Convergence of the solution facing non-linear adhesive deformations. Convergence of the Finite Element models.

Figure A2-5. Evolution of the maximum displacement at loaded nodes as a function of the number of elements within the length of the adhesive bondline. Convergence of the solution facing linear-elastic adhesive deformations. Convergence of the semi-analytical models.

Figure A2-6. Evolution of the adhesive peel and shear stresses at crack tip as a function of the number of elements within the length of the adhesive bondline. Convergence of the solution facing linear-elastic adhesive deformations. Convergence of the semi-analytical models.

Figure A2-7. Evolution of the maximum displacement at loaded nodes as a function of the number of elements within the length of the adhesive bondline. Convergence of the solution facing non-linear adhesive deformations. Convergence of the semi-analytical models.

Figure A2-8. Evolution of the adhesive peel and shear stresses at crack tip as a function of the number of elements within the length of the adhesive bondline. Convergence of the solution facing non-linear adhesive deformations. Convergence of the semi-analytical models.

Figure 1. Schematic representation of the local equilibrium of the bonded adherends. Linear elastic 1D-beam model.

Figure 2. Definition of the nodal displacements and the nodal forces acting on the BBe element. Linear elastic 1D-beam model.

Figure 3. Restriction to bi-linear (a), exponential (b), polynomial (c), and perfectly plastic (d) softening behavior. However the procedure is not limited to these particular behaviors only. Cohesive zone model.

Figure 4. Graphical representation of the mixed-mode parameters. Description of the mixed-mode I/II adhesive behavior.

Figure 5. False position method. Computation of the effective initiation/propagation properties of the adhesive layer. Combination of the pure modes adhesive behaviors.

Figure 6. Dissimilar left side and right side adhesive secant stiffnesses. Computation of the secant stiffness matrix K_S. Adaptation of the Newton-Raphson procedure. Computation of the vector of imbalanced loads.

Figure 7. Schematic representation of ENF, DCB & MMB adhesive specimens. Description of the Finite Element models.

Figure 8. Schematic representation of ENF, DCB & MMB adhesive specimens. Description of the semi-analytical models.

Figure 9. Comparison between semi-analytical results and Finite Element analyses. End-Notched Flexure specimen. Confrontation with classical Finite Element analyses.

Figure 10. Comparison between semi-analytical results and Finite Element analyses. Double Cantilever Beam specimen. Confrontation with classical Finite Element analyses.

Figure 11. Comparison between semi-analytical results and Finite Element analyses. Mixed-Mode Bending specimen. Confrontation with classical Finite Element analyses.

Figure 12. Comparison between semi-analytical and Finite Element converged predictions. Evaluation of the total number of degrees of freedom.

LIST OF TABLES

APPENDIX 1 - STIFFNESS MATRIX OF A SINGLE-LAP JOINT

A1.1. Stiffness matrix of the outer adherends

The equations of local equilibrium of beams outside the overlap are written as follows:

$$\begin{cases} \dfrac{dN_j}{dx} = 0 \\ \dfrac{dV_j}{dx} = \qquad\qquad , j = 1,2 \\ \dfrac{dM_j}{dx} + V_i = 0 \end{cases} \tag{A-1}$$

In addition to the constitutive equations of adherends (equation (2)), the stiffness matrix of a beam element – denoted $\boldsymbol{K_{Beam}}$ – can be computed following the same method as the one described in section 2. The stiffness matrix of the single beam element can be finally written as follows:

$$\mathbf{K}_{\mathbf{Beam}} = \begin{pmatrix} \frac{A_j}{l_j} & -\frac{A_j}{l_j} & 0 & 0 & -\frac{B_j}{l_j} & \frac{B_j}{l_j} \\ -\frac{A_j}{l_j} & \frac{A_j}{l_j} & 0 & 0 & \frac{B_j}{l_j} & -\frac{B_j}{l_j} \\ 0 & 0 & \frac{12}{l_j^3}\frac{\Delta}{A_j} & -\frac{12}{l_j^3}\frac{\Delta}{A_j} & \frac{6}{l_j^2}\frac{\Delta}{A_j} & \frac{6}{l_j^2}\frac{\Delta}{A_j} \\ 0 & 0 & -\frac{12}{l_j^3}\frac{\Delta}{A_j} & \frac{12}{l_j^3}\frac{\Delta}{A_j} & -\frac{6}{l_j^2}\frac{\Delta}{A_j} & -\frac{6}{l_j^2}\frac{\Delta}{A_j} \\ -\frac{B_j}{l_j} & \frac{B_j}{l_j} & \frac{6}{l_j^2}\frac{\Delta}{A_j} & -\frac{6}{l_j^2}\frac{\Delta}{A_j} & \frac{1}{l_j}\left(3\frac{\Delta}{A_j} + D_j\right) & \frac{1}{l_j}\left(3\frac{\Delta}{A_j} - D_j\right) \\ \frac{B_j}{l_j} & -\frac{B_j}{l_j} & \frac{6}{l_j^2}\frac{\Delta}{A_j} & -\frac{6}{l_j^2}\frac{\Delta}{A_j} & \frac{1}{l_j}\left(3\frac{\Delta}{A_j} - D_j\right) & \frac{1}{l_j}\left(3\frac{\Delta}{A_j} + D_j\right) \end{pmatrix} , j = 1,2 \tag{A-2}$$

A1.2. Stiffness matrix of the single lap joint

The stiffness matrix of the entire single-lap joint is then assembled from the elementary stiffness matrices $\boldsymbol{K_{BBe}}$ and $\boldsymbol{K_{Beam}}$, according to the classical FE rules (see Fig.A-1).

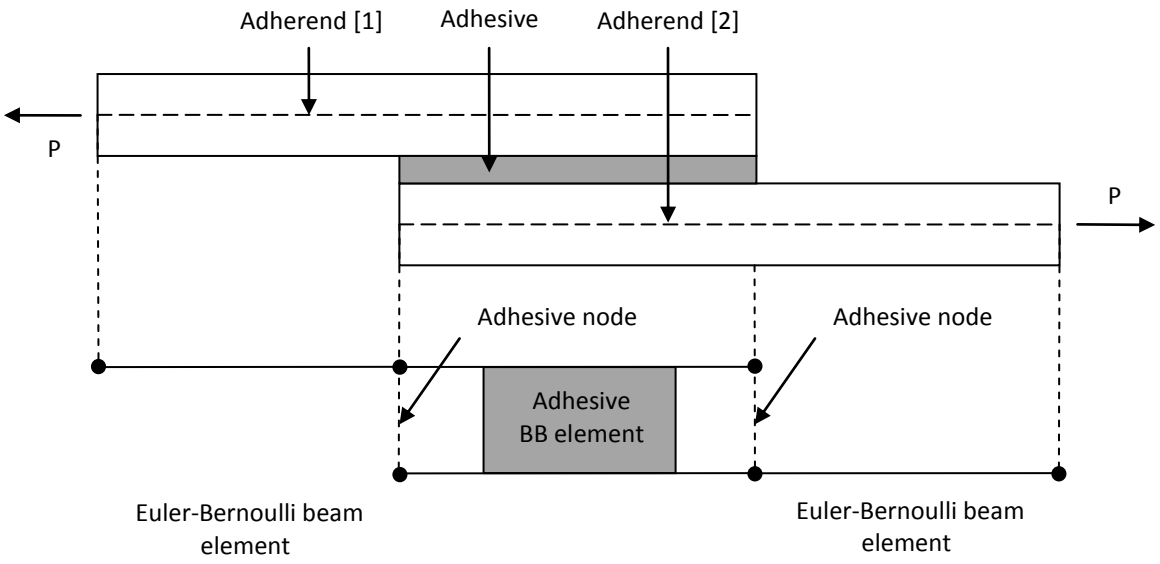

Figure A1-1. Assembly of the single-lap joint configuration. Linear elastic 1D-beam model.

APPENDIX 2 – CONVERGENCE OF THE NUMERICAL RESULTS

A2.1. Convergence of the Finite Element models

Convergence of the linear-elastic FE results. Since the DCB[3] specimen has been largely shown as the critical configuration in term of convergence of the numerical results, the results are then presented for this configuration only. Fig.A2-1 then shows the evolution of the maximum displacement at loaded nodes as a function of the number of elements within the length of the adhesively bonded overlap of the DCB[3] specimen facing linear-elastic deformations only. Fig.A2-2 shows the evolution of the adhesive peel and shear stresses at crack tip as a function of the number of elements within the length of the adhesively bonded overlap of the same specimen. It is seen from Fig.A2-1 and Fig.A2-2 that the linear elastic analyses clearly converge towards an asymptote.

Convergence of the non-linear FE results. Fig.A2-3 shows the evolution of the maximum displacement at loaded nodes as a function of the number of elements within the length of the adhesively bonded overlap of the DCB[3] specimen facing non-linear adhesive deformations. Fig.A2-4 shows the evolution of the adhesive peel and shear stresses at crack tip as a function of the number of elements within the length of the adhesively bonded overlap of the same specimen. In comparison to linear elastic analyses, the non-linear solutions do not appear as clearly converging toward an asymptote (see Fig.A2-3 and Fig.A2-4). However, and since SAMCEF uses a Newton-Raphson based procedure to account for the non-linear behavior of the adhesive layer, the converged results can be noised by the inherent convergence criterion. The number of elements within the length of the overlap is then fixed to 200 for both the ENF[2], the DCB[3], and the MMB[4] specimens.

A2.2. Convergence of the semi-analytical models

Convergence of the linear-elastic semi-analytical results. Fig.A2-5 shows the evolution of the maximum displacement at loaded nodes as a function of the number of elements within the length of the adhesively bonded overlap of the DCB[3] specimen facing linear-elastic deformations only. Fig.A2-6 shows the evolution of the adhesive peel and shear stresses at crack tip as a function of the number of elements within the length of the adhesively bonded overlap of the same specimen. It is seen from Fig.A2-5 and Fig.A2-6 that the linear elastic semi-analytical analyses are clearly independent on the mesh refinement.

Convergence of the non-linear semi-analytical results. Fig.A2-7 shows the evolution of the maximum displacement at loaded nodes as a function of the number of elements within the length of the adhesively bonded overlap of the DCB[3] specimen facing non-linear adhesive deformations. Fig.A2-8 shows the evolution of the adhesive peel and shear stresses at crack tip as a function of the number of elements within the length of the adhesively bonded overlap of the same specimen. In comparison to linear elastic analyses, the non-linear solutions appear as depending on the mesh refinement. However, it is seen from Fig.A2-7 and Fig.A2-8 that the non-linear solutions rapidly converge towards an asymptote. The number of BBe elements within the length of the overlap is then fixed to 200 for both the ENF[2], the DCB[3], and the MMB[4] specimens.

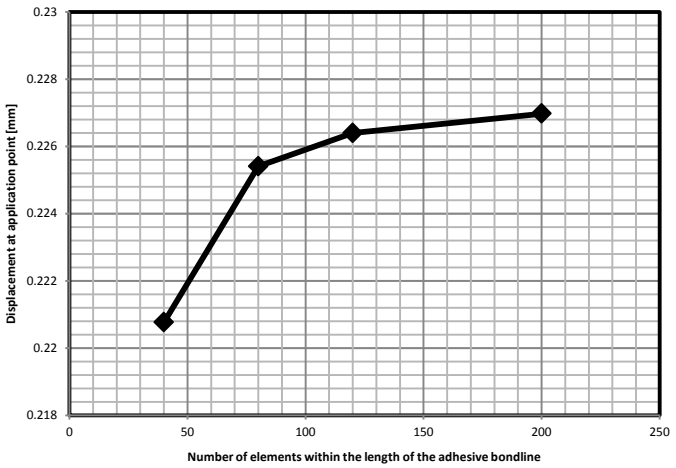

DCB specimen

Figure A2-1. Evolution of the maximum displacement at loaded nodes as a function of the number of elements within the length of the adhesive bondline. Convergence of the solution facing linear-elastic deformations. Convergence of the Finite Element models.

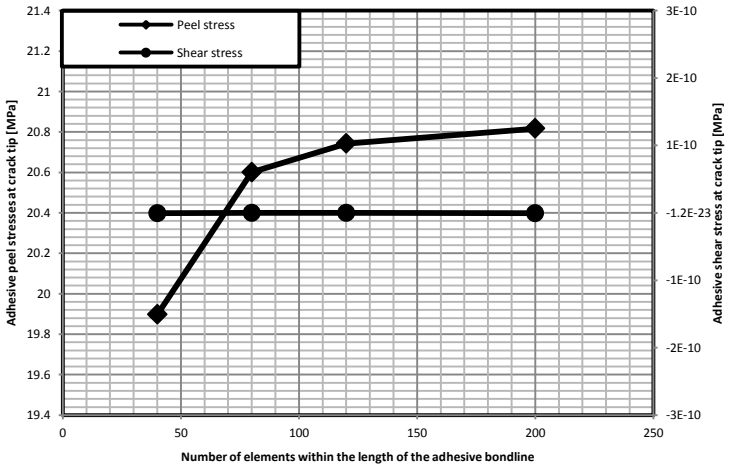

DCB specimen

Figure A2-2. Evolution of the adhesive peel and shear stresses at crack tip as a function of the number of elements within the length of the adhesive bondline. Convergence of the solution facing linear-elastic adhesive deformations. Convergence of the Finite Element models.

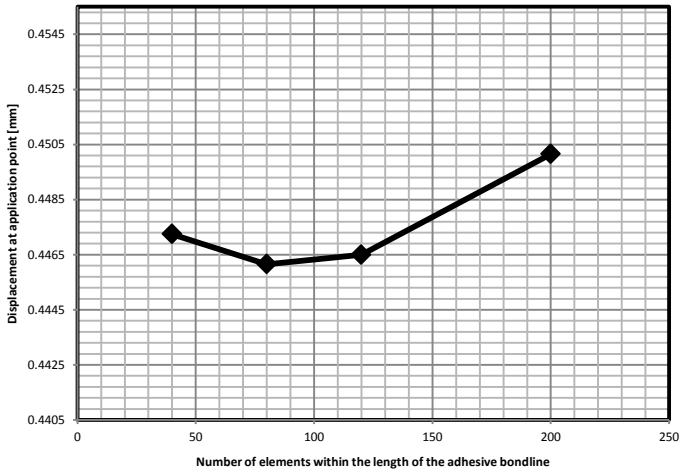

DCB specimen

Figure A2-3. Evolution of the maximum displacement at loaded nodes as a function of the number of elements within the length of the adhesive bondline. Convergence of the solution facing non-linear adhesive deformations. Convergence of the Finite Element models.

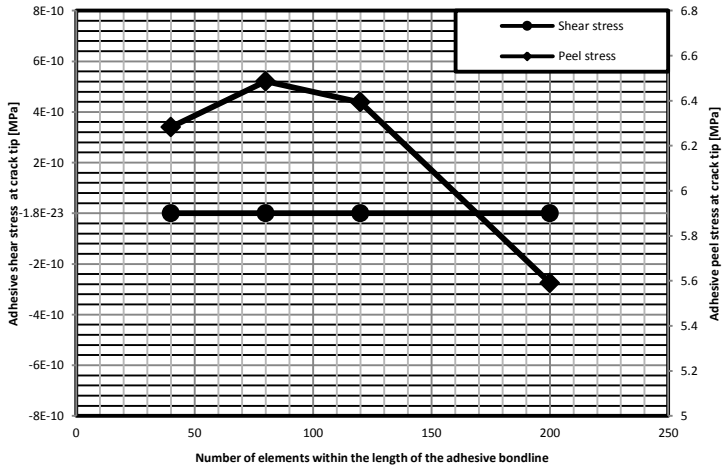

DCB specimen

Figure A2-4. Evolution of the adhesive peel and shear stresses at crack tip as a function of the number of elements within the length of the adhesive bondline. Convergence of the solution facing non-linear adhesive deformations. Convergence of the Finite Element models.

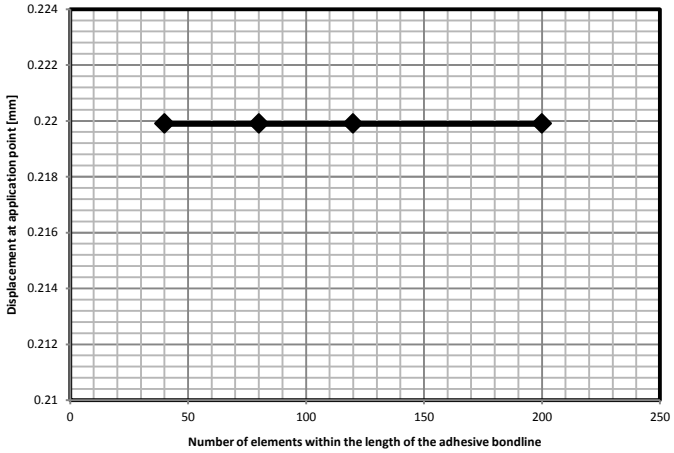

DCB specimen

Figure A2-5. Evolution of the maximum displacement at loaded nodes as a function of the number of elements within the length of the adhesive bondline. Convergence of the solution facing linear-elastic adhesive deformations. Convergence of the semi-analytical models.

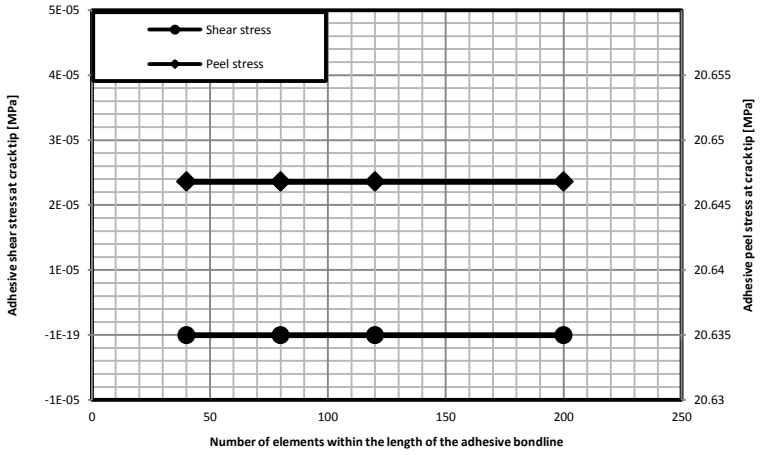

DCB specimen

Figure A2-6. Evolution of the adhesive peel and shear stresses at crack tip as a function of the number of elements within the length of the adhesive bondline. Convergence of the solution facing linear-elastic adhesive deformations. Convergence of the semi-analytical models.

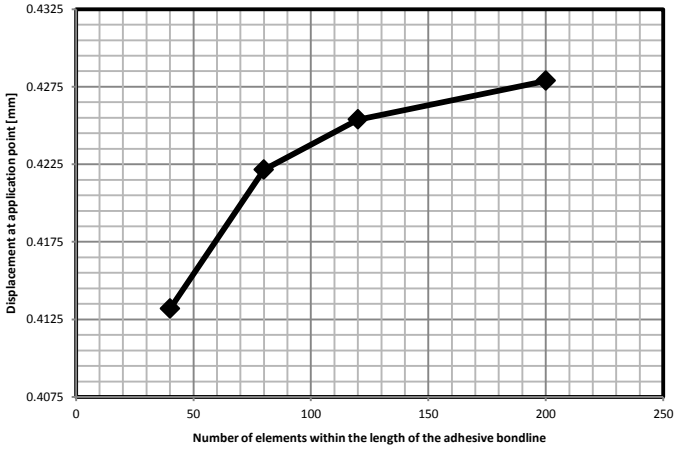

DCB specimen

Figure A2-7. Evolution of the maximum displacement at loaded nodes as a function of the number of elements within the length of the adhesive bondline. Convergence of the solution facing non-linear adhesive deformations. Convergence of the semi-analytical models.

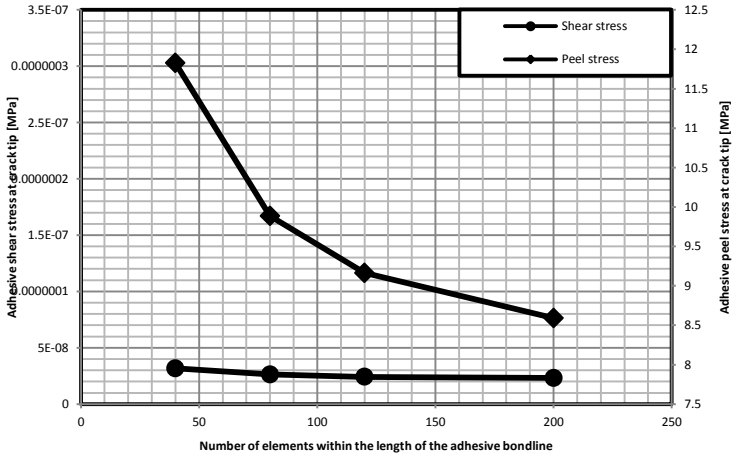

DCB specimen

Figure A2-8. Evolution of the adhesive peel and shear stresses at crack tip as a function of the number of elements within the length of the adhesive bondline. Convergence of the solution facing non-linear adhesive deformations. Convergence of the semi-analytical models.

Figures

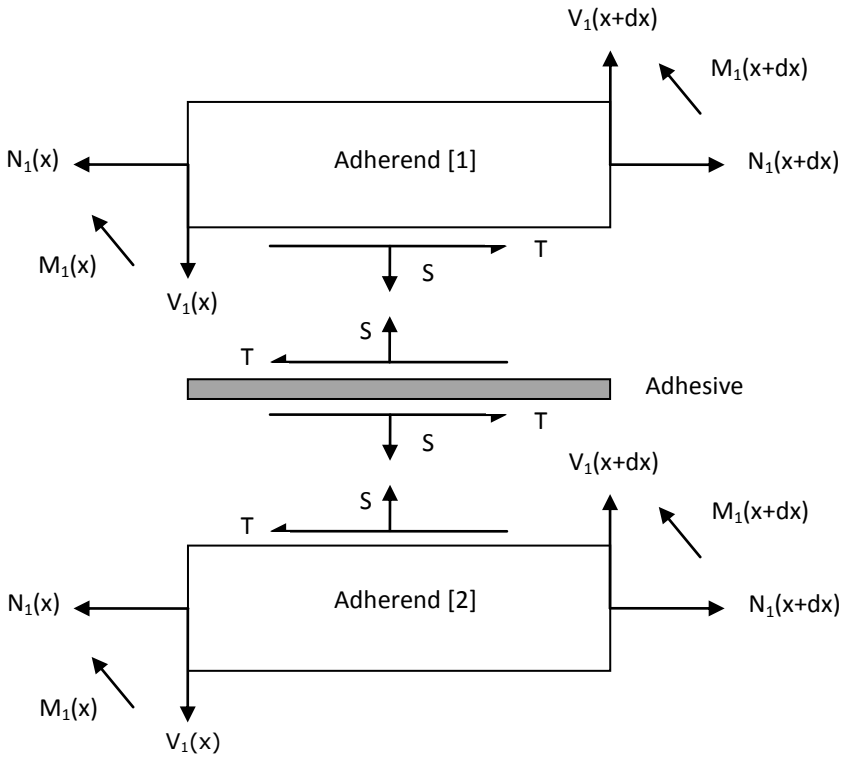

N_j : Normal force of adherend (j) [N] ; V_j : Shear force of adherend (j) [N] ; M_j : Bending moment of adherend (j) [Nm] ; T : Adhesive shear stress [Mpa] ; S : Adhesive peel stress [Mpa] ;

Figure 1. Schematci representation of the local equilibrium of the bonded adherends. Linear elastic 1D-beam model.

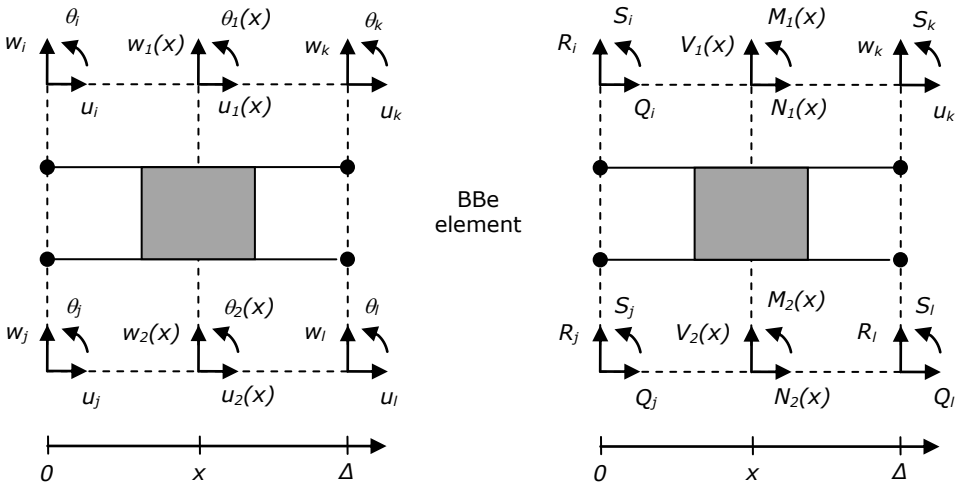

u_j : normal displacement of adherend (j) [mm] ; w_j : transverse displacement of adherend (j) [mm] ; θ_j : bending angle of adherend (j) [rad] ; N_j : Normal force of adherend (j) [N] ; V_j : Shear force of adherend (j) ; M_j : Bending moment of adherend (j) [Nm] ;

Figure 2. Definition of the nodal displacements and the nodal forces acting on the BBe element. Linear elastic 1D-beam model.

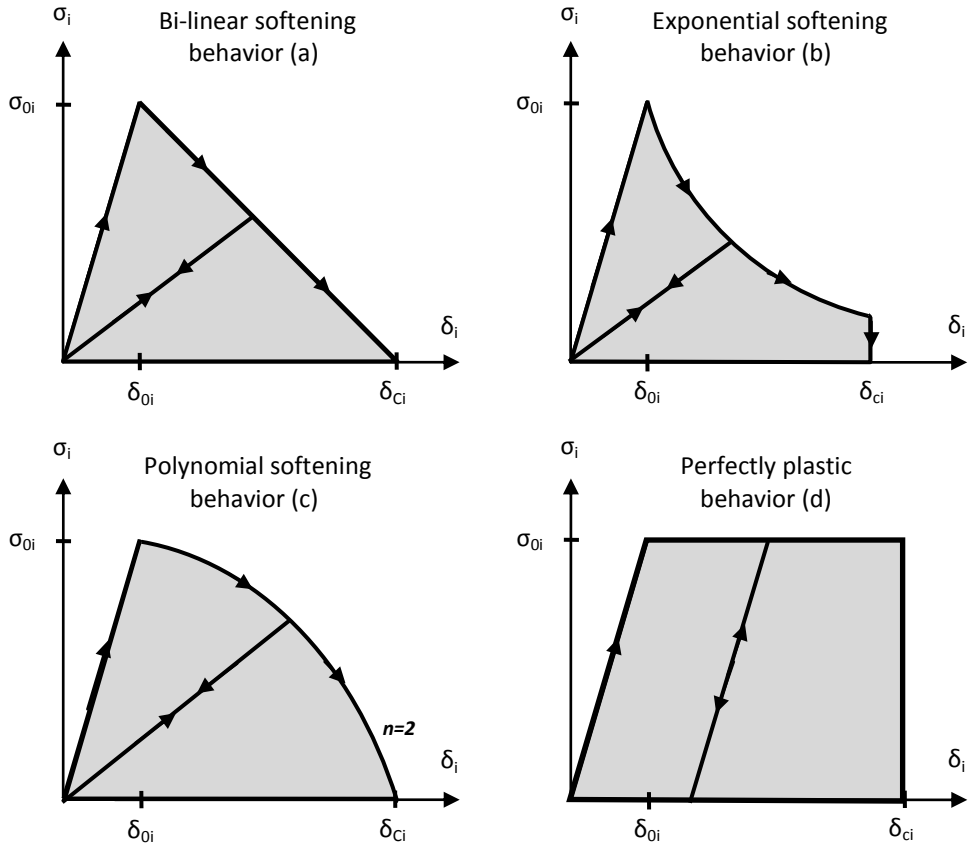

Figure 3. Restriction to bi-linear (a), exponential (b), polynomial (c), and perfectly plastic (d) softening behavior. However the procedure is not limited to these particular behaviors only. Cohesive zone model.

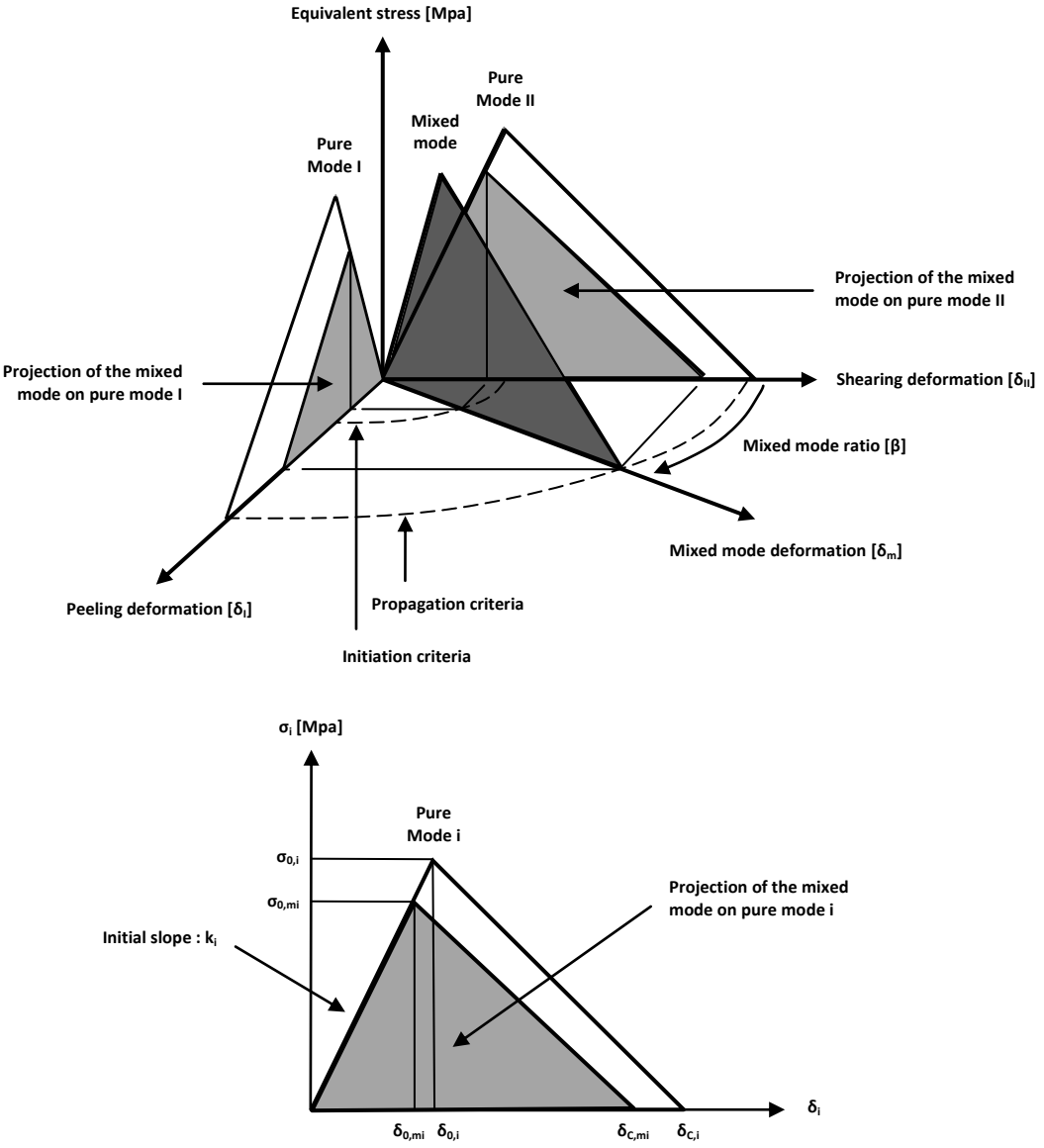

Figure 4. Graphical representation of the mixed-mode parameters. Description of the mixed-mode I/II adhesive behavior.

Tab 1. Examples of initiation/propagation mixed-mode criteria. Description of the pure mode adhesive behavior.

Linear energetic criterion [12]	Benzeggagh-Kenane criterion [24]
$\frac{G_{C,mI}}{G_{C,I}} + \frac{G_{C,mII}}{G_{C,II}} - 1 = 0$	$G_{C,I}\left(G_{C,II} - G_{C,I}\right)\left(\frac{G_{C,mII}}{G_{C,mI} + G_{C,mII}}\right)^{\eta} - \left(G_{C,mI} + G_{C,mII}\right) = 0$
Quadaratic energetic criterion [25]	JR Reeder criterion [23]
$\left(\frac{G_{C,mI}}{G_{C,I}}\right)^2 + \left(\frac{G_{C,mII}}{G_{C,II}}\right)^2 - 1 = 0$	$G_{C,I} + \rho\left(\frac{G_{0,mII}}{G_{0,II}}\right) + \upsilon\left(\frac{G_{0,mII}}{G_{0,II}}\right)^2 - \left(G_{C,mI} + G_{C,mII}\right) = 0$

Tab 2. Mathematical representation of classical softening behaviors. Description of the pure mode adhesive behavior.

i=(I,II)	Linear elastic representation ($\delta_i<\delta_{0,i}$)	Non-linear softening representation ($\delta_{0,i}<\delta_i<\delta_{C,i}$)
Linear elastic	$\sigma_i(\delta_i) = k_i\delta_i$	N.A
Bi-linear cohesive damage	$\sigma_i(\delta_i) = k_i\delta_i$	$\sigma_i(\delta_i) = \left[1 - \left(1 - \frac{\delta_{0,i}(\delta_{C,i} - \delta_i)}{\delta_i(\delta_{C,i} - \delta_{0,i})}\right)\right] k_i\delta_i$
Polynomial cohesive damage	$\sigma_i(\delta_i) = k_i\delta_i$	$\sigma_i(\delta_i) = \left[1 - \left(1 - \frac{\delta_{0,i}(\delta_{C,i}^n - \delta_i^n)}{\delta_i(\delta_{C,i}^n - \delta_{0,i}^n)}\right)\right] k_i\delta_i$
Exponential cohesive damage	$\sigma_i(\delta_i) = k_i\delta_i$	$\sigma_i(\delta_i) = \left[1 - \left(1 - exp(1 - \delta_i/\delta_{0,i})\right)\right] k_i\delta_i$
Perfectly plastic cohesive damage	$\sigma_i(\delta_i) = k_i\delta_i$	$\sigma_i(\delta_i) = \left[1 - \left(1 - \frac{\delta_{0,i}}{\delta_i}\right)\right] k_i\delta_i$

Tab 3. Mathematical description of the elastic energy ($Y_{0,i}$) and the fracture energy ($G_{C,i}$) of pure mode i ($i=II$). Description of the pure mode adhesive behavior.

i=(I,II)	Elastic Energy ($Y_{0,i}$)	Fracture Energy ($G_{C,i}$)
Linear elastic	$Y_{0,i} = \frac{1}{2}k_i\delta_{0,i}^2$	N.A
Bi-linear cohesive damage	$Y_{0,i} = \frac{1}{2}k_i\delta_{0,i}^2$	$G_{C,i} = Y_{0,i}\left[1 + \left(\frac{\delta_{C,i}}{\delta_{0,i}} - 1\right)\right] = \frac{1}{2}k_i\delta_{0,i}\delta_{C,i}$
Polynomial cohesive damage	$Y_{0,i} = \frac{1}{2}k_i\delta_{0,i}^2$	$G_{C,i} = Y_{0,i}\left[1 + 2\frac{\delta_{C,i}^n(\delta_{C,i} - \delta_{0,i})}{\delta_{0,i}(\delta_{C,i}^n - \delta_{0,i}^n)}\left(1 - \frac{1}{n+1}\frac{(\delta_{C,i}^{n+1} - \delta_{0,i}^{n+1})}{\delta_{C,i}^n(\delta_{C,i} - \delta_{0,i})}\right)\right]$
Exponential cohesive damage	$Y_{0,i} = \frac{1}{2}k_i\delta_{0,i}^2$	$G_{C,i} = Y_{0,i}\left[5 - 2\left(\frac{\delta_{C,i}}{\delta_{0,i}} + 1\right)exp\left(1 - \frac{\delta_{C,i}}{\delta_{0,i}}\right)\right]$
Perfectly plastic cohesive damage	$Y_{0,i} = \frac{1}{2}k_i\delta_{0,i}^2$	$G_{C,i} = Y_{0,i}\left[1 + 2\left(\frac{\delta_{C,i}}{\delta_{0,i}} - 1\right)\right]$

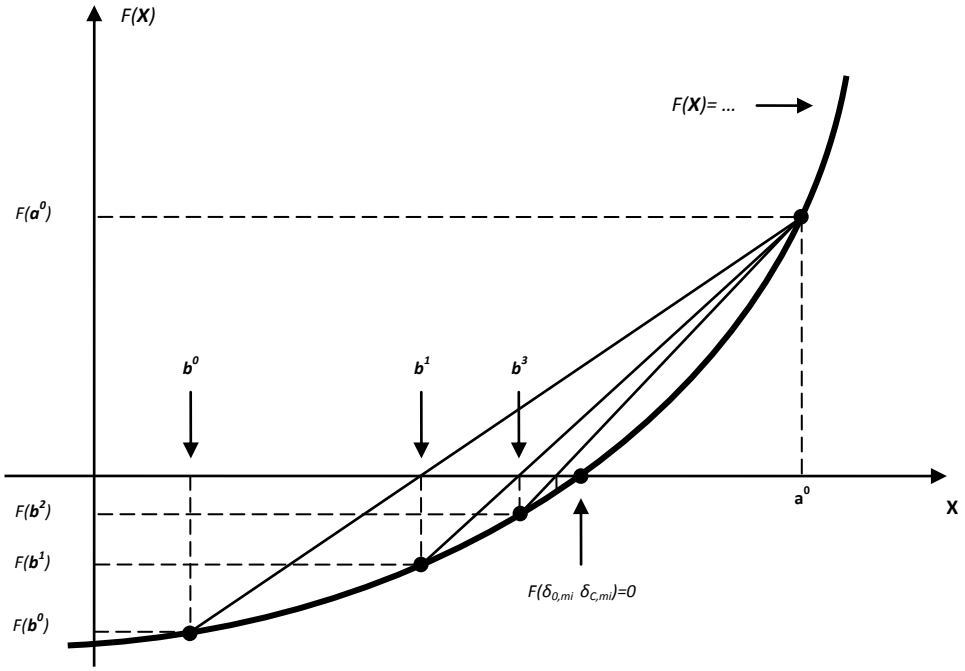

Figure 5. False position method. Computation of the effective initiation/propagation properties of the adhesive layer. Combination of the pure modes adhesive behaviors.

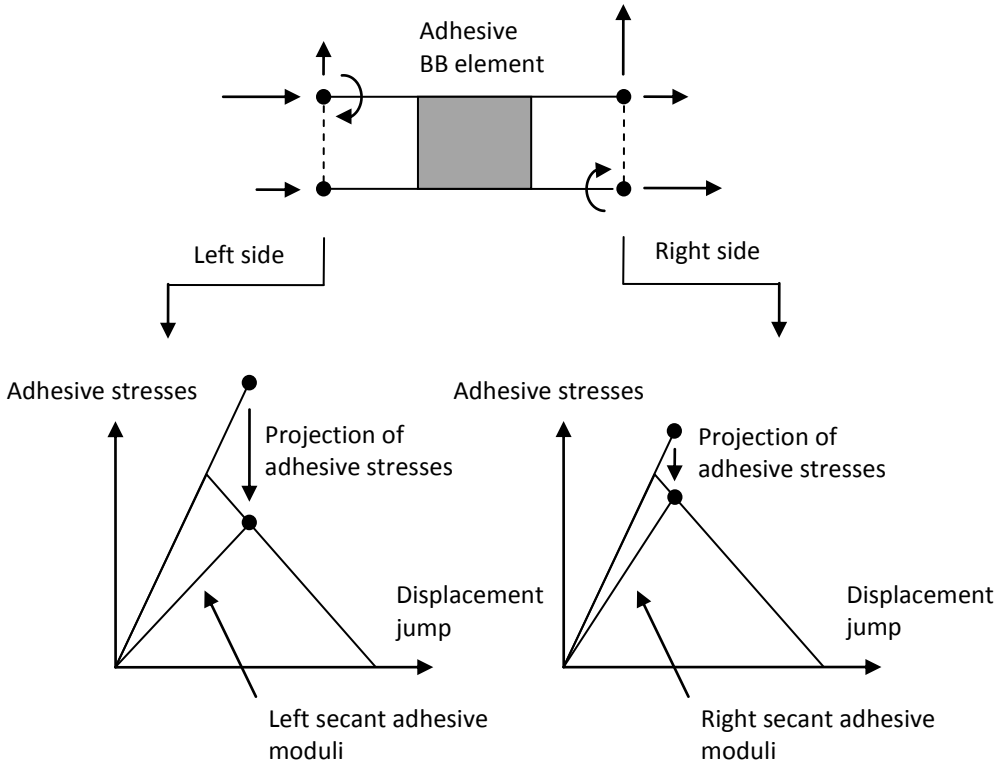

Figure 6. Dissimilar left side and right side adhesive secant stiffnesses. Computation of the secant stiffness matrix K_S. Adaptation of the Newton-Raphson procedure. Computation of the vector of imbalanced loads.

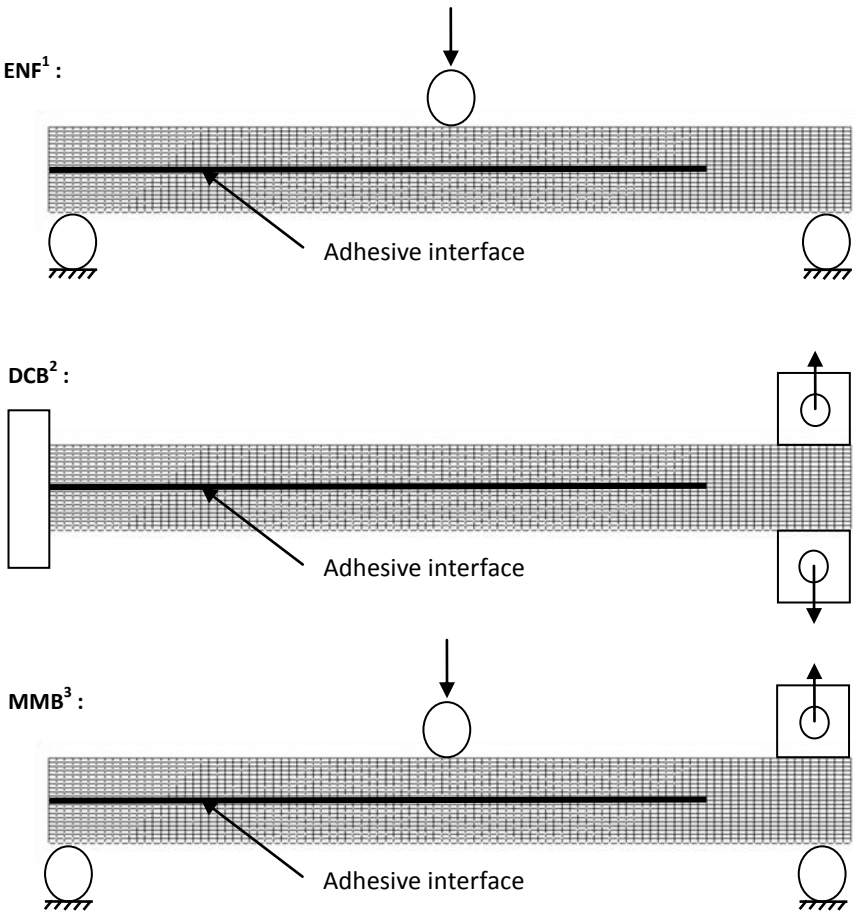

Figure 7. Schematic representation of ENF, DCB & MMB adhesive specimens. Description of the Finite Element models.

Tab 4. Adherend elastic properties. Initial and effective* mechancial properties. Description of the Finite Element models.

Adherends elastic properties.			
E	74200 Mpa	E^*	66120. Mpa
G	27900 Mpa	G^*	24860. Mpa
ν	0.34	ν^*	-

Tab 5. Adhesive mechanical properties. Description of the Finite Element models.

Adhesive properties.			
k_I	185 Mpa	k_{II}	65 Mpa
$Y_{0,I}$	2. J/mm^2	$Y_{0,II}$	2. J/mm^2
$G_{C,I}$	4. J/mm^2	$G_{C,II}$	5. J/mm^2
Initiation criteria	Linear energetic	Propagation criteria	Linear energetic

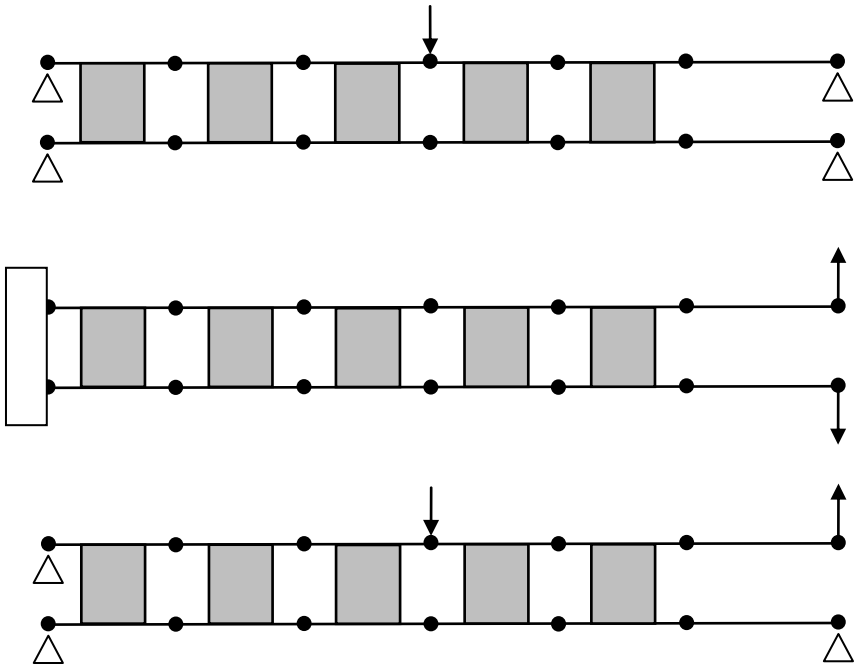

Figure 8. Schematic representation of ENF, DCB & MMB adhesive specimens. Description of the semi-analytical models.

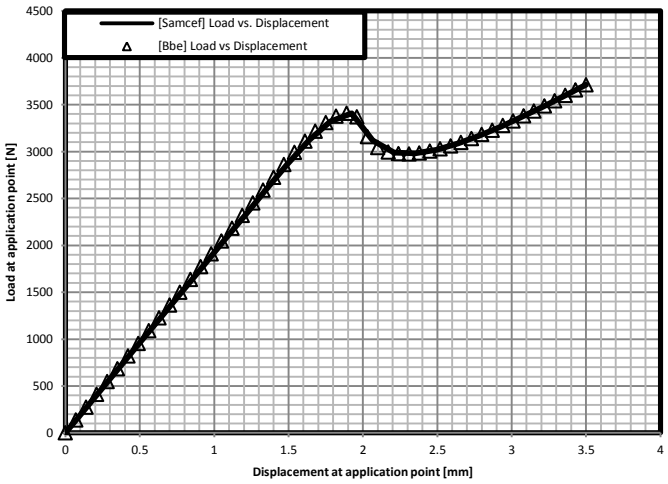

Load versus displacement (a)

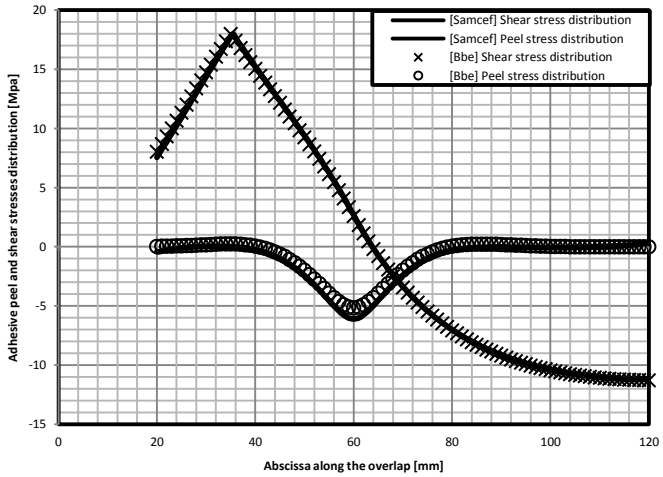

Adhesive shear and stress distributions (b)

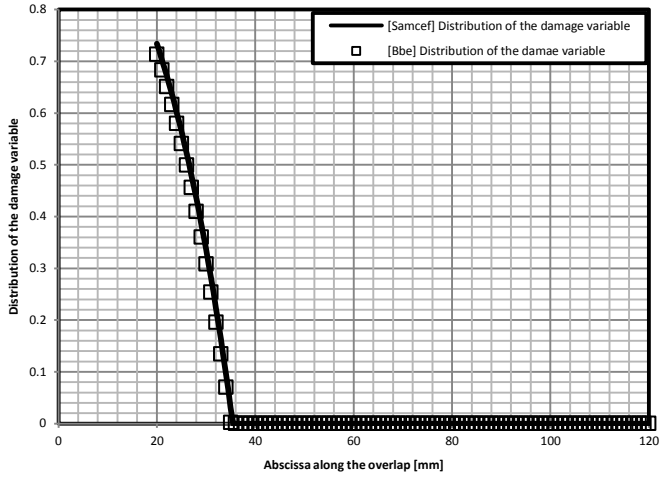

Distribution damage variable (c)

Figure 9. Comparison between semi-analytical results and Finite Element analyses. End-Notched Flexure specimen. Confrontation with classical Finite Element analyses.

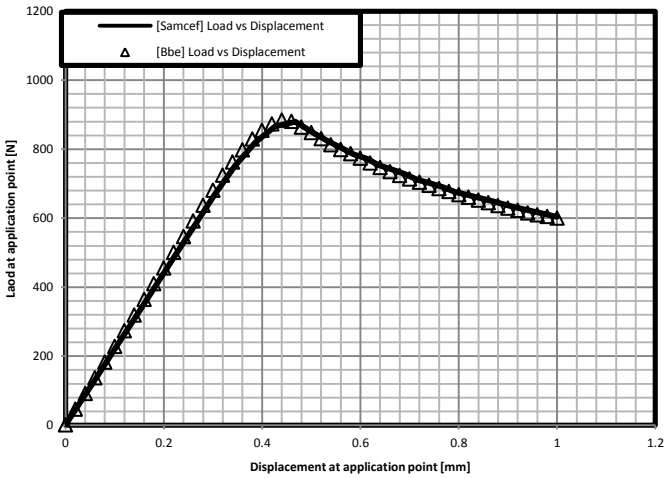

Load versus displacement (a)

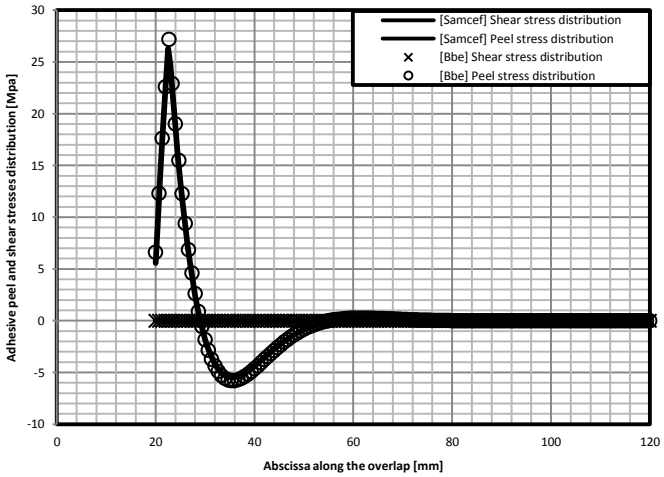

Adhesive shear and stress distributions (b)

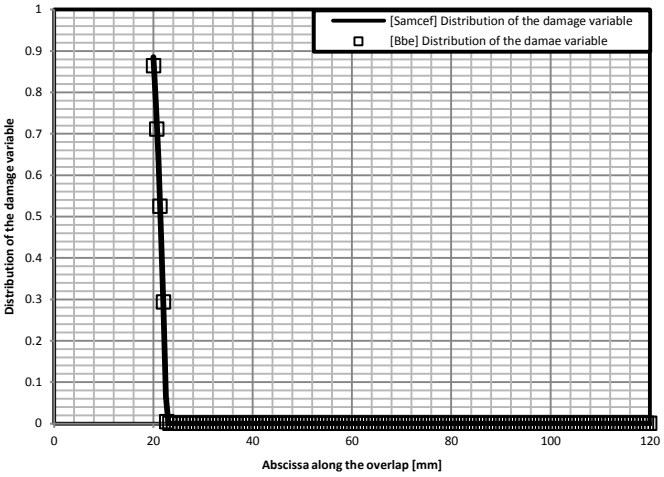

Distribution damage variable (c)

Figure 10. Comparison between semi-analytical results and Finite Element analyses. Double Cantilever Beam specimen. Confrontation with classical Finite Element analyses.

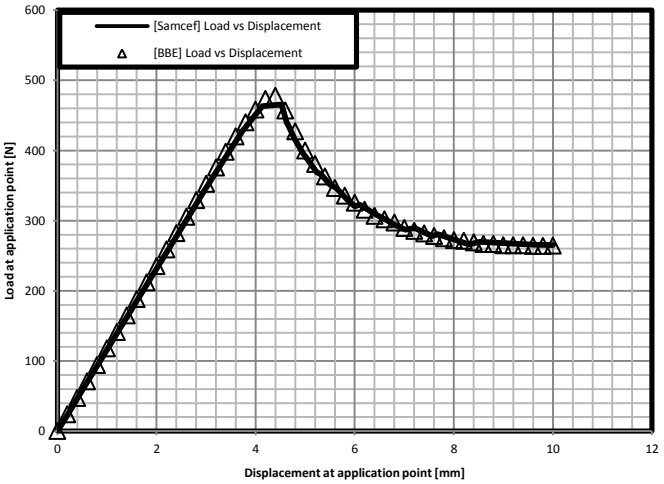

Load versus displacement (a)

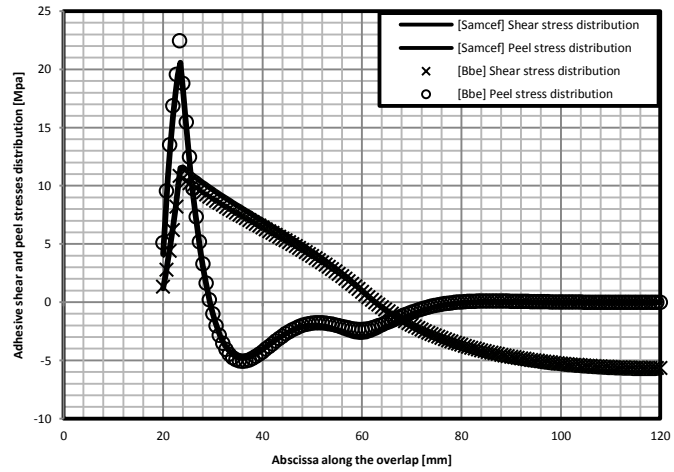

Adhesive shear and stress distributions (b)

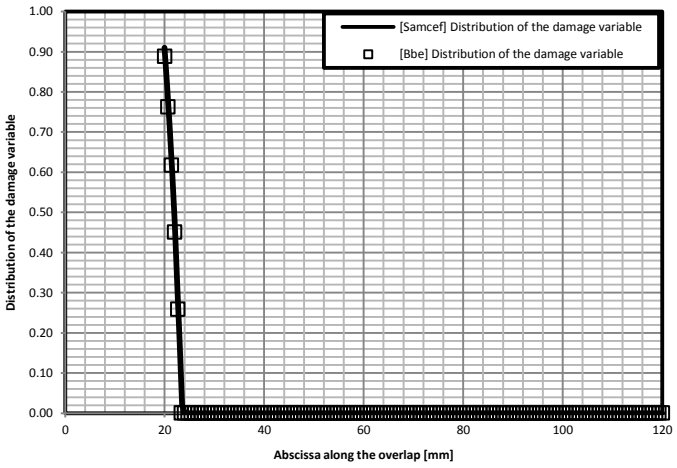

Distribution damage variable (c)

Figure 11. Comparison between semi-analytical results and Finite Element analyses. Mixed-Mode Bending specimen. Confrontation with classical Finite Element analyses.

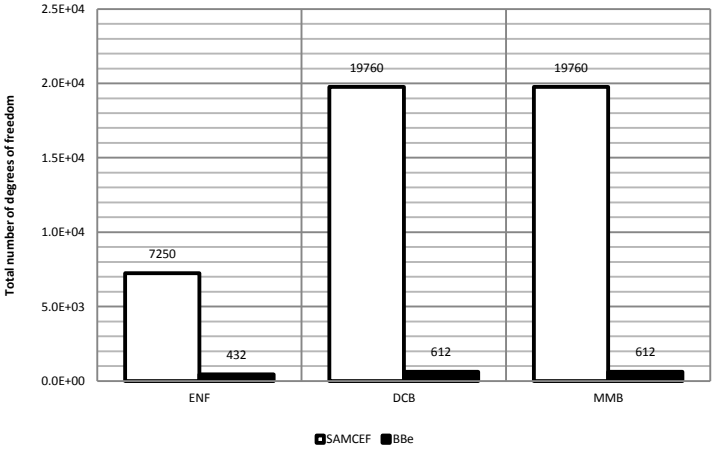

Figure 12. Comparison between semi-analytical and Finite Element converged predictions. Comparison of the total number of degrees of freedom.